Reviewed Preprint
v1 • September 16, 2025
Not revised

Reviewed Preprint
v2 • June 3, 2026
Revised by authors

For correspondence:
metzler-baddeleyc@cardiff.ac.uk

Competing interests: No competing interests declared

Funding: See page 30

Reviewing editor: Jason P Lerch, University of Oxford, United Kingdom

In vivo mapping of striatal neurodegeneration in Huntington's disease with Soma and Neurite Density Imaging

Vasileios Ioakeimidis[1,2], Marco Palombo[1], Chiara Casella[3,4,5], Lucy Layland[1], Carolyn B McNabb[1], Robin Schubert[6], Philip Pallmann[7], Monica E Busse[7], Cheney JG Drew[7], Sundus Alusi[8], Timothy Harrower[9], Jane Davies[10], Anne E Rosser[11,12], Claudia Metzler-Baddeley[1]

[1]Cardiff University Brain Research Imaging Centre (CUBRIC), School of Psychology, Cardiff University, Cardiff, United Kingdom • [2]Danish Research Centre for Magnetic Resonance, Department for Radiology and Nuclear Medicine, Copenhagen University Hospital Amager and Hvidovre, Copenhagen, Denmark • [3]Department for Forensic and Neurodevelopmental Sciences, Institute of Psychiatry, Psychology and Neuroscience, King's College London, London, United Kingdom • [4]Early life imaging research department, School of Biomedical Engineering and Imaging Sciences, King's College London, London, United Kingdom • [5]London Collaborative Ultra high field System (LoCUS), Kings College London, London, United Kingdom • [6]George Huntington Institut (GHI), Muenster, Germany • [7]Centre for Trials Research, School of Medicine, Cardiff University, Cardiff, United Kingdom • [8]The Walton Centre for Neurology and Neurosurgery, Liverpool, United Kingdom • [9]Royal Devon and Exeter NHS Trust, Exeter, United Kingdom • [10]Cardiff and Vale University Health Board, Main University Hospital Wales Building, Cardiff University, Cardiff, United Kingdom • [11]Cardiff University Brain Repair Group, School of Biosciences, Cardiff University, Cardiff, United Kingdom • [12]Advanced Neurotherapeutics Centre (ANTC), Department of Neurology and Psychological Medicine, School of Medicine, Cardiff University, Cardiff, United Kingdom

eLife Assessment

This **fundamental** manuscript presents a novel application of the SANDI (Soma and Neurite Density Imaging) model to study microstructural alterations in the basal ganglia of individuals with Huntington's disease (HD). The **compelling** methods are, to our understanding, the first application of SANDI to neurodegenerative diseases, provide strong evidence for HD-related neurodegeneration in the striatum, account significantly for striatal atrophy, and correlate with motor impairments. The integration of novel diffusion acquisition and modelling methods with multimodal behavioural data are both of high value in their own right, and create a framework for future studies.

https://doi.org/10.7554/eLife.107661.2.sa3

Abstract

Background Huntington's Disease (HD) is an inherited neurodegenerative disorder characterised by progressive cognitive and motor decline resulting from atrophy within basal ganglia networks. Although no disease-modifying therapies currently exist, several novel clinical trials are ongoing. Sensitive non-invasive imaging biomarkers are therefore essential for evaluating therapeutic effects. Soma and Neurite Density Imaging (SANDI), a multi-shell diffusion-weighted imaging model, estimates intracellular signal fractions arising from sphere-shaped soma that show promise as proxies for HD-related neurodegeneration. Although HD is rare, it offers a

valuable model for understanding other neurodegenerative diseases due to its clear genetic cause and shared patterns of protein abnormalities.

Objective To characterise HD-related microstructural abnormalities in the basal ganglia and thalami using SANDI and examine associations between SANDI indices, volumetric measurements, and motor performance.

Methods T1-weighted anatomical and multi-shell diffusion-weighted images (b-values: 200 s/mm²– 6,000 s/mm²) were acquired using a 3T Siemens Connectom scanner (300mT/m) in 56 HD individuals ($Mean_{Age}$ = 46.1, SD_{Age} = 13.8, 25 females) and 57 healthy controls ($Mean_{Age}$ = 45.0, SD_{Age} = 13.8, 31 females). HD participants completed Quantitative Motor (Q-Motor) tasks, including speeded and paced finger tapping, which were reduced to one principal component of motor performance. Following standard diffusion-weighted data preprocessing, SANDI and diffusion tensor models estimated apparent soma density, apparent soma size, apparent neurite density, extracellular signal fraction, fractional anisotropy, and mean diffusivity. The caudate, putamen, pallidum, and thalamus were segmented bilaterally, and micro-structural and volumetric indices were extracted and compared. Correlations between SANDI indices, Q-Motor performance, and volumetric measures were analysed.

Results HD was associated with reduced apparent soma density (r_{rb} = 0.32, $p \leq 0.007$) and increased apparent soma size (r_{rb} = 0.45, $p < 0.001$) and extracellular signal fraction (r_{rb} = 0.34, $p \leq 0.003$) in the basal ganglia, but not the thalami. These differences were more pronounced at HD-Integrated Staging System 0-1 than 2-3. No differences were found in apparent neurite density (r_{rb} = 0.18, p = 0.17). HD-related increases in fractional anisotropy and mean diffusivity in the basal ganglia were replicated. Q-Motor component scores correlated negatively with apparent soma density and positively with apparent soma size and extracellular signal fraction. SANDI indices and age explained up to 63% of striatal atrophy in HD.

Conclusion SANDI measures detected HD-related neurodegeneration in the striatum, accounted significantly for striatal atrophy, and correlated with motor impairments. Reduced apparent soma density and increased apparent soma size align with *ex vivo* evidence of medium spiny neuron loss and glial reactivity. SANDI shows promise as an *in vivo* biomarker and surrogate outcome measure for clinical trials of disease-modifying therapies for HD and other neurodegenerative diseases.

Introduction

Huntington's disease (HD) is an autosomal dominantly inherited neurodegenerative disorder caused by a pathogenic CAG repeat expansion of the Huntingtin gene.[1] HD is characterised by a progressive loss of cognitive and motor functions as well as psychiatric disturbances.

The clinical onset of HD is commonly defined by the manifestation of motor symptoms, such as chorea, reduced voluntary motor control, bradykinesia, and difficulty maintaining rhythmic and paced movements.[2–4] However, changes in the brain, notably striatal atrophy in the basal ganglia (BG)[5,6] may precede the motor onset by up to 24 years[7–10] and correlate with motor and cognitive decline.[2,5,6,11–15] While HD is rare (~12 in 100,000), it can be seen as a model neurodegenerative disorder, due to its clear genetic cause, well-characterized disease progression, and shared features of protein abnormalities with more common disorders like Alzheimer's and Parkinson's disease.[5]

There is presently no approved disease-modifying therapy for HD, but several clinical trials are underway to test the safety and efficacy of novel therapeutics.[16] The recent surge in potential disease-modifying targets has generated a demand for surrogate outcome measures that are sensitive to HD neuropathology and allow a mechanistic assessment of therapeutic effects on striatal neurodegeneration in a timely manner. Volumetric measurements from non-invasive MRI are known to be sensitive to disease progression[17–20] and have been adopted into the Huntington's Disease Integrated Staging System (HD-ISS).[21] However, volumetric measurements do not provide

information about the underlying neuropathological tissue changes that lead to striatal atrophy, such as the loss of medium spiny neurons (MSN)[22,23] and changes in glia cell density and morphology, including enlargement of reactive astrocytes and microglia.[22,24–26]

Diffusion-weighted Imaging (DWI) is widely used to investigate brain tissue microstructure *in vivo* by exploiting apparent water displacement due to Brownian motion.[27,28] Most DWI studies in HD have used diffusion tensor imaging (DTI), which models extra-cellular water diffusion as a Gaussian tensor and measures diffusion properties such as mean diffusivity (MD) and the degree of diffusion anisotropy (fractional anisotropy; FA).[29] DTI studies in HD have consistently reported increases in MD and FA in striatal grey matter,[30,31] that likely arise from the selective neurodegeneration of MSN connections.

Advances in multi-shell and ultra-strong gradient DWI,[32] have enabled increasingly sophisticated biophysical models that require data acquisition over a range of b-values to separate extra- from intracellular diffusion signals.[33–35] Several approaches that model intraneurite space with cylinders or sticks have been put forward (e.g. Composite and Restricted Model of Diffusion, CHARMED[33]; Convex optimization modelling for microstructure informed tractography; COMMIT[36]; Neurite Orientation Dispersion and Density Index; NODDI[34]). NODDI studies in premanifest HD have revealed reduced apparent neurite density in white mater with localised reductions in fibre orientation dispersion in the corpus callosum and basal ganglia capsules.[37] However, despite putamen volume loss, no NODDI-based differences in striatal grey matter were detected in gene-positive individuals long before motor onset.[10]

Soma And Neurite Density Imaging (SANDI)[38] is a diffusion MRI model that extends biophysical multi-compartment models to capture microstructural features of cell bodies and processes *in vivo*. SANDI requires multi-shell acquisition protocols with b-values over 3,000 s/mm^2 to capture intracellular restricted signal fractions. Biologically, its parameters describe the relative contributions of somas, neurites (axons, dendrites and glial processes), and extracellular space to the diffusion-weighted MRI signal: the soma signal fraction (f_{is}) reflects the density of neuronal and glial cell bodies, the neurite fraction (f_{in}) captures density of axons, dendrites and glial processes, and the extracellular fraction (f_{extra}) and extracellular diffusivity (D_e) account for the surrounding milieu. The MR apparent soma radius (r_s) further provides an estimate of (volume-weighted) average cell body size. Mathematically, SANDI models the diffusion signal attenuation as a weighted combination of restricted diffusion in spheres (somas), restricted diffusion in cylinders of infinitesimally small radius (neurites), and Gaussian diffusion in the extra-cellular compartment, constrained by the condition that the compartment fractions sum to one. These parameters thus provide biologically interpretable and mathematically well-defined indices of cellular composition, enabling non-invasive characterization of brain microstructure beyond what can be achieved with conventional diffusion models.

SANDI has been shown to provide highly reproducible and repeatable parameter estimation across grey matter regions in the human brain[39] that align closely with its known cyto- and myeloarchitecture. For instance, the gradients of apparent soma density maps were found to closely match those of Brodmann areas in human cortical regions with different soma density profiles,[38] and correlated in the mouse brain with cell density distributions from the Allen atlas.[38,40] These findings suggest the potential of the SANDI model for quantifying neurodegenerative processes in the grey matter of the living human brain.

Clinical applications of SANDI have so far been limited to multiple sclerosis (MS) and amyotrophic lateral sclerosis (ALS). In MS, reductions in apparent soma and neurite density, together with increases in extracellular signal fraction, have been reported in both grey and white matter, consistent with demyelination, axonal loss, and neurodegeneration.[41,42] These abnormalities correlated with disease severity,[42,43] cortical and subcortical atrophy,[41,44] and elevated serum neurofilament light chain levels, a marker of axonal damage[44] that is also sensitive to HD progression.[45,46] Similar patterns, namely reduced apparent soma density and region-specific alterations in apparent soma size have recently been observed in ALS, [43] aligning with motor neuron loss and glial responses.

The primary objective of this study was to determine whether SANDI indices were sensitive and specific to microstructural grey matter differences in the BG, compared with the thalami, in individuals with HD relative to healthy controls. The thalami were selected as control regions based on the established trajectory of neurodegeneration in HD, which begins with early loss of MSN in the striatum before extending to neighbouring structures such as the putamen and thalamus. At most participants were at early disease stages, we assumed the thalami would remain relatively unaffected in this sample.

Secondary objectives were to explore the extent to which HD-related SANDI differences accounted for BG atrophy, assessed using volumetric measurements, and for performance differences in motor tasks, including speeded and paced finger tapping, which are known to be associated with striatal atrophy in HD. [47] Finally, relationships between SANDI indices and disease burden using the HD-ISS [21] and the CAG-Age Product (CAP_{100}) score [48] were explored.

Materials and methods

Participants

MRI data from 56 individuals with HD and 57 age- and sex-matched healthy controls (HC) were included in the analyses. Imaging data were retrospectively pooled from three projects, all of which acquired scans on the same Siemens Connectom system at the Cardiff University Brain Research Imaging Centre (CUBRIC) using identical acquisition protocols. Thirty-eight of the HD participants were drawn from a randomised controlled feasibility trial of HD-DRUM,[49] a remote rhythmic training intervention, with ethical approval from the Wales Research Ethics Committee 2 (REC Reference: 22/WA/0147).[55] Here we report their baseline MRI and behavioural data collected prior to randomisation. An additional 18 individuals with HD and 18 age-matched HC were included from a previous study of white matter microstructure in premanifest HD (REC Reference: 18/WA/0172).[50] Further comparison data were obtained from 25 age- and sex-matched HC from the Wales Advanced Neuroimaging Database (WAND) Study[51] (REC Reference: 18.08.14.5332RA3) and 14 HC from the HD-DRUM trial. All participants provided written informed consent in accordance with the Declaration of Helsinki.

HD individuals were identified and screened for eligibility in five clinics in the UK (Bristol, Birmingham, Cardiff, Exeter, and Liverpool). HC volunteers were recruited from online advertisements on the Cardiff University social network, Viva Engage, or in HD clinics as support partners or family members. HC participants were also recruited through *Healthwise Wales* and by word of mouth. For the WAND study, data collection was reported elsewhere.[51]

Individuals aged 18 years or older with a good command of English were eligible to participate. Additional inclusion criteria for individuals with HD[49] were a positive genetic test for the presence of the mutant huntingtin allele (CAG length ≥ 36 repeats) and/or clinical diagnosis of HD, along with a Unified Huntington's Disease Rating Scale (UHDRS) Total Functional Capacity (TFC) score between 9 and 13.[52] Exclusion criteria for all participants included an inability to provide informed consent and any contraindication for MRI (e.g. pacemakers, stents). Further exclusion criteria were a history of any other neurological condition for HD participants, and for HC, a history of neurological or psychiatric disorders, and/or alcohol or drug abuse associated with grey matter volume loss.

To characterise general cognitive functioning, HD participants completed the Montreal Cognitive Assessment (MOCA).[53] Verbal intellectual ability was assessed using the Test of Premorbid Functioning (TOPF).[54] Disease burden was estimated by the TFC score and the CAG-Age Product (CAP100) score,[48] calculated as:

$$CAP_{100} = Age * \frac{CAG-30}{6.49}$$

HD-ISS[21] staging and associated clinical information for stratification were obtained from the Enroll-HD[55] observational study (former Registry; REC no 04/WSE05/89). However, due to the retrospective pooling of datasets, HD-ISS information was available for only 30 HD participants (see Supplementary Table 1 for demographic and clinical characteristics).

Motor outcome measures

Participants in the HD-DRUM study completed a range of motor tasks from the Quantitative-Motor (Q-Motor) test-battery,[56–58] which provided reliable assessments of speeded finger tapping performance in clinical HD trials.[59,60] Tasks included left and right 1) speeded index finger and foot tapping using force transducers,[47] 2) paced finger and foot tapping[47] with a metronome-paced and memory-paced phase, using a fast (0.55s inter-onset interval; IOI) or slow (1.1s IOI) pace, 3) 3D pointing to four target locations in a predefined sequence using a position-tracking stylus with the dominant hand[61] and 4) 3D target pointing and speeded finger tapping dual task performed with dominant and non-dominant hand, respectively. Outcome measures included mean IOI (seconds) and area under the curve (AUC) (Newton-seconds) for the speeded tapping, mean absolute deviation from the metronome pace (seconds) for the paced tapping, target frequency (Hz) for the target pointing, and target frequency, mean IOI and AUC for the dual-task condition.

Image acquisition

All MRI data included in the analyses were acquired on the same 3T Siemens Connectom scanner (Siemens Healthcare, Erlangen, Germany) with ultra-strong magnetic gradients (300mT/m) at CUBRIC using identical acquisition protocols as detailed below. No scanner changes or upgrades were performed during the data collection periods.

T1-weighted (T1w) images were acquired using a magnetisation-prepared 180-degrees radio-frequency pulses and rapid gradient-echo (MPRAGE), with the following parameters: repetition time (TR) 2,300 ms, echo time (TE) 2 ms, field of view (FOV) 256 x 256 x 192 mm, matrix size 256 x 256 x 192, resolution 1 x 1 x 1 mm^3, flip angle 9°, inversion time (TI) 857 ms, in-plane acceleration (GeneRalised Autocalibrating Partial Parallel Acquisition; GRAPPA) factor 2, phase-encoding direction anterior to posterior (AP), and acquisition time of 6 minutes.

Multi-shell High Angular Resolution Diffusion Imaging (HARDI)[62] data were obtained at b-values of 200 s/mm^2 (20 directions), 500 s/mm^2 (20 directions), 1,200 s/mm^2 (30 directions). 2,400 s/mm^2 (61 directions), 4,000 s/mm^2 (61 directions) and 6,000 s/mm^2 (61 directions) using a single-shot spin-echo, echo-planar imaging sequence with TR = 3,000 ms, TE = 59 ms, FOV 220 x 200 mm in-plane; matrix size 110 x 110 x 66; 2 mm^3 resolution, gradient pulse duration - δ = 7 ms, gradient pulses separation - Δ = 24 ms in AP phase-encoding direction with an in-plane acceleration (GRAPPA) factor of 2. Fifteen non-diffusion-weighted (b-value = 0 s/mm^2) images were acquired [two initial and 11 interspersed at the 33^{rd} volume and every 20^{th} volume thereafter in AP direction and 2 images in the posterior-to-anterior (PA) direction]. The HARDI acquisition time was 18 minutes.

Image processing

Diffusion-weighted image preprocessing

Multi-shell HARDI data were pre-processed and corrected for signal drift, susceptibility-induced distortions, motion and eddy current-induced distortions, gradient non-uniformity and Gibbs ringing artifacts using a custom in-house pipeline comprising tools from the FMRIB Software Library (FSL version 6.0.3),[63] the MRtrix software package,[64] ExploreDTI[65] (version 4.8.6) and in-house MATLAB-based scripts.[39]

The FSL brain extraction tool[63] was used to mask the first non-diffusion-weighted image from each phase-encoding direction to exclude non-brain data. The diffusion-weighted MRI volumes were fitted to temporally interspersed b0 volumes to correct for within-image intensity drift by using custom code in MATLAB R2017b (MathWorks Inc., Natick, Massachusetts, USA). Slicewise outlier detection (SOLID)[66] was applied with modified Z-score thresholds of 3.5 (lower) and 10 (upper), utilising a variance-based intensity metric. FSL's top-up tool[67,68] was used to estimate susceptibility-induced off-resonance fields from b0 images that were acquired in opposing phase-encoding directions (AP and PA) and then FSL's eddy tool[69] was used to correct eddy current-

induced distortions and subject movements. Gradient non-uniformity distortions were corrected using in-house code in MATLAB R2017b. Finally, Gibbs ringing correction was performed in MRtrix3 using the local subvoxel-shifts method.[70]

For the purpose of comparing our results with the previous literature,[30] DTI was fitted with ExploreDTI using data with b-values of 500 s/mm² and 1,200 s/mm² to produce outcome maps for FA and MD, estimated with linearly weighted least squares regression.

SANDI analysis

The SANDI model [38] assumes three compartments, namely intra-neurite signal modelled as diffusion inside impermeable randomly oriented sticks, intra-soma signal modelled as restricted diffusion inside spheres, and extra-cellular signal modelled as Gaussian isotropic diffusion. The direction-averaged (or spherical mean) normalized diffusion signal has thus the following expression:

$$S(b) = f_{is}A_{\text{sphere}}\ (b, r_s, D_{is}) + f_{in}A_{\text{stick}}\ (b, D_{in}) + f_{ec}A_{\text{ball}}\ (b, D_e)$$

where $f_{in} + f_{is} + f_{ec} = 1$; A_{stick} and A_{sphere} are the normalized, directionally-averaged (or spherical mean) signals for restricted diffusion within neurites and soma, respectively and A_{ball} is the normalized, directionally-averaged (or spherical mean) signal of the extra-cellular space. The specific expressions are given in [38].

The parameters estimated from the direction-averaged (or spherical mean) data are D_{in}, proxy of the intra-neurite effective axial diffusivity; D_e, proxy of the extracellular effective mean diffusivity; r_s, a proxy of apparent soma radius as well as the signal fractions subject to the constraint $f_{in} + f_{is} + f_{ec} = 1$, proxy respectively of the relaxation-weighted neurite, soma and extracellular volume fractions. The bulk diffusivity inside the sphere D_{is} is fixed to 3 μm^2/ms.

The parameters were fitted using a Random Forest regression algorithm (TreeBagger Matlab®) with 200 trees, trained on simulated data, using the code publicly available at *https://github.com/palombom/SANDI-Matlab-Toolbox-Latest-Release*. The training data consisted of simulated signals for 10^5 parameter combinations, uniformly sampled: f_{in} and $f_{is} \in [0, 1]$, $D_{in} \in [0.5, 3]$ μm^2/ms, $D_e \in [0.5, 3]$ μm^2/ms and $r_s \in [1, 12.5]$ μm. Rician noise with a distribution of standard deviations randomly sampled from the voxels within the brain mask of the noise map was obtained using Marchenko-Pastur principal component analysis (MP-PCA)-based method[71–73] in MRtrix3 and was added to account for realistic SNR levels and rectified noise floor. The loss function of the training was the mean squared error between predicted parameters and ground truth values. These noise maps were subsequently used to fit the SANDI model[38] to the pre-processed multi-shell diffusion data with the SANDI MATLAB Toolbox (*https://github.com/palombom/SANDI-Matlab-Toolbox-Latest-Release*[38] using all the default settings.

The model fitting produced maps of the intra-neurite, extracellular and intra-soma signal fractions (f_{in}, f_{ec}, f_{is}), apparent soma size (r_s; measured in μm) and intra- and extra-neurite diffusivities (D_{in}, D_e; measured in mm^2/ms). Post-hoc sensitivity analysis of the SANDI model parameters revealed very low sensitivity to changes in D_{in}. Consequently, it was excluded from further analysis.

T1-weighted image preprocessing

The default FreeSurfer [74] (v6) *recon-all* pipeline was utilised to segment subcortical BG ROIs of the caudate, putamen, and globus pallidum as well as of the thalamus as control ROIs. ROIs were segmented from T1w images and were identified and labelled in each hemisphere.

Extraction of microstructural metrics from regions-of-interest

Median values of each microstructural index from DTI (FA, MD) and SANDI (f_{is}, f_{in}, f_{ec}, r_s, D_e) models were extracted for each ROI using FSL's *fslmaths*. ROI masks were aligned with the diffusion space using rigid transformation with FSL's *flirt*[75] before eroding the boundaries of the subcortical masks by one voxel with the default 3 × 3 × 3 kernel settings to minimise partial volume effects and then aligning all microstructural maps with the masks.

Volumetric measures for each ROI and intra-cranial volume (ICV) were extracted from FreeSurfer v6 ROI volumes were normalised for ICV. The addition of brain volumes allowed exploration of the extent to which any HD-related SANDI differences accounted for BG atrophy.

Statistical analysis

Statistical analyses were performed in JASP (v0.18.1.0)[76], R version 4.4.1 (2024-06-14)[77] in R-studio (2024.9.0.375)[78] and SPSS (v27) (IBM Corp).[79] Data normality was assessed using the Shapiro-Wilk test, with $p < 0.05$ indicating non-normal distribution. Descriptive statistics for each group were reported as percentages (%), means and standard deviations (SD). Medians of each microstructural index in each ROI were compared between the groups with Mann-Whitney-U tests because of lack of normality and unequal variance between groups. Effect sizes (ES) for group comparisons were therefore reported with rank biserial correlation (r_{rb}). Multiple comparisons were corrected with Benjamini-Hochberg's method to control a false discovery rate (FDR) of 0.05[80] and applied to all statistical tests that related to the same theoretical inference.[81]

Multi-collinearity of imaging metrics was explored by calculating the intercorrelations between all SANDI, DTI, and volumetric measurements averaged across all four ROIs (caudate, putamen, pallidum, and thalamus). Spearman's rho (ρ) correlation matrices were calculated in the full sample, as well as the HC and HD groups separately.

Hierarchical linear regression analyses were conducted to explore SANDI predictors of the variance in volumetric measurements. Regression analyses were carried out for each ROI and each group separately. HD data were modelled by firstly accounting for age and TFC scores (available for all HD participants) simultaneously. This was followed by step-wise inclusion of all SANDI indices using an iterative forward selection and backward elimination method based on each variable's F-statistic and p-value that aimed to maximise the adjusted R^2-value while keeping only the most significant predictors. HD and HC data were modelled in the same way using all SANDI variables and age, except for the inclusion of TFC scores that were only available for HD participants.

Principal Component Analysis (PCA) was carried out to reduce the dimensionality of HD participants' Q-Motor data and hence the number of multiple correlations with microstructural SANDI indices. PCA followed established guidelines to limit the number of extracted components in relatively small sample sizes.[82,83] First the Kaiser criterion of including all components with an eigenvalue greater than 1 was applied and the Cattell scree plot was inspected to identify the minimal number of components that accounted for most variability in the data. Each extracted component was then assessed for interpretability. PCA was conducted using orthogonal Varimax rotation of the component matrix with Kaiser normalization. Loadings that were greater than 0.5 were considered to be statistically significant.

Spearman's rho (ρ) correlations were then calculated between HD participants' motor component scores and the CAP100 with the SANDI indices, DTI, and volumetric measures in each ROI.

HD-ISS categories were obtained either directly from Enroll-HD or calculated using the online HD-ISS calculator (*https://enroll-hd.org/calc/html_basic.htm*) based on caudate and putamen volumes derived from the FreeSurfer v6[74] cross-sectional pipeline. For participants labelled "<2" in the Enroll-HD database (reflecting missing imaging data), we distinguished between stages 0 and 1 using two complementary approaches. First, adjusted normative modelling was applied, in which caudate and putamen volumes from healthy controls were modelled using linear regression with age, sex, and ICV as covariates, and individual z-scores were generated from model residuals. Second, raw group-based normalisation was performed by z-scoring ICV-normalised volumes relative to the control mean and SD. Participants labelled "<2" were classified as HD-ISS 1 if either adjusted caudate or putamen z-scores fell ≥ 2 SD below the control mean; otherwise, they were assigned to stage 0. Both approaches produced identical classifications.

Explorative analyses of HD-ISS-related differences in SANDI indices were conducted for BG ROIs. Due to small sample sizes, participants at Stages 0 and 1 were combined (HD-ISS 0-1), as were those at Stage 2 and 3 (HD-ISS 2-3). SANDI metrics for each ROI were averaged across hemispheres.

Pairwise comparisons between HD-ISS 0-1 versus HC, HD-ISS 0-1 versus HD-ISS 2-3, and HD-ISS 2-3 versus HC were performed using Mann–Whitney U tests without additional FDR correction.

Results

Demographics

Sample characteristics, including age and sex distribution for the HD and HC groups are described in Table 1. The groups were comparable with regards to age and sex (p>0.05).

Information for HD-ISS calculation was available for 30 individuals. Of these 4 were stratified into Stage 0, 9 into Stage 1, 5 into Stage 2, and 12 into Stage 3; no participants were classified as Stage 4. One individual could not be assigned a stage because their clinical presentation did not align with the HD-ISS assumption that motor symptoms precede functional decline. An additional, 25 individuals could not be classified due to missing clinical data or CAG repeat lengths between 36-39. Demographic and clinical characteristics for each HD-ISS stage, as well as for unclassified participants are summarised in Supplementary Table 1. Supplementary Table 2 provides descriptive statistics for the Q-Motor measures.

Imaging analysis

Differences between HD and HC groups in volumetric measures

Table 2 summarises the volumetric group differences across the eight ROIs with their ES. Figure 1 illustrates the ES maps of volumetric differences between HD and HC, as well as raincloud plots for each ROI. Mann-Whitney tests identified significantly reduced volumes in all BG ROIs in HD compared to HC with moderate ES (r_{rb} = 0.46-0.55). In contrast, no reductions were present in the right (*FDR-p* = .05) and left thalamus (*FDR-p* = .063) (both r_{rb} = 0.2).

Differences between HD and HC groups in microstructural measures

Descriptive and statistical microstructural results are shown in Table 3. Figure 2 provides ES mappings and raincloud plots of the different microstructural measures for each ROI comparing the two groups.

The SANDI measures revealed between-group differences in apparent soma density, apparent soma size, and extracellular signal fraction with moderate ES in the BG (r_{rb} = 0.32-0.53) (Fig. 2). HD individuals exhibited reduced apparent soma density (Fig. 2A) across all BG ROIs. Apparent soma size was elevated in bilateral caudate and putamen but reduced in the pallidum (Fig. 2B). Elevated extracellular signal fraction was observed in all BG regions (Fig. 2C). Extracellular diffusivity was higher in the putamen and pallidum but not in the caudate (Fig. 2D). No differences were observed for apparent neurite density f_{in} in any of the ROIs (*FDR-p* ≥ 0.167, absolute r_{rb} < 0.2).

Increased FA and MD (*FDR-p* < 0.01) with moderate ES (r_{rb} = 0.30-0.61) were observed in the BG (Fig. 2E-F) with the exception of MD in the left pallidum (*FDR-p* = 0.854).

No differences were found in the thalami for any of the microstructural metrics (*rrb* = 0.02-0.19).

Correlations between BG microstructure and motor performance in HD

Motor measures

PCA extracted one principal component that explained 64% of the Q-Motor data with high loadings (> 0.5 or <-0.5) from all variables (Supplementary Table 3). Spearman's rho correlation between Q-motor component scores and the disease burden CAP_{100} score revealed a positive correlation (ρ = 0.61, p = 0.002, N = 24), i.e., higher disease burden was associated with higher scores in the Q-Motor component reflecting slower and less accurate motor performance (Supplementary Figure 1).

Table 1. **Demographic and clinical information of participants**

	HD group		HC group		*Statistic* (*p-value*)
	N	Mean (SD)	*N*	Mean (SD)	
Age	56	46.12 (13.79)	57	44.96 (13.75)	$t_{(111)} = 0.446$ (0.657)
Female, N (%)		25 (44.7%)		31 (54.4%)	$\chi^2 = 1.073$ (0.300)
Education (years)	38	14.16 (2.58)	14	15.86 (2.54)	$t_{(50)} = 2.06$ (0.448)
HD-ISS stage 0/1/2/3, N_{total}		4/9/5/12, 30			
MOCA	55	26.47 (3.55)		-	
TOPF	56	49.70 (13.16)		-	
UHDRS-TFC	56	12.11 (1.25)		-	
UHDRS-TMS	51	11.03 (15.82)		-	
CAG	50	41.82 (2.67)		-	
CAP	50	80.55 (22.60)		-	
SDMT	38	45.47 (14.91)			

Abbreviations: **CAG**: Cytosine Adenine Guanine; **CAP**: CAG-Age-Product; **HC**: Healthy Controls; **HD**: Huntington's Disease; **HD-ISS**: Huntington's Disease International Staging System; **MOCA**: Montreal Cognitive Assessment; **SD**: Standard Deviation; **SDMT**: Symbol Digit Modalities Test; **TFC**: Total Functional Capacity; **TMS**: Total Motor Score; **TOPF**: Test Of Premorbid Functioning; **UHDRS**: United Huntington's Disease Rating Scale

Figure 1. **Volumetric differences in the basal ganglia and thalamus between HD and healthy control (HC) groups.**

Regions-of-interest (ROIs) were segmented using FreeSurfer v6. All ROIs, except the left thalamus, showed significantly smaller volumes in the HD cohort after FDR correction for multiple comparisons. Colours indicate the strength of rank-biserial correlations (r_{rb}) from Mann-Whitney U tests: Red = strong effect ($r_{rb} \geq 0.5$), Yellow = medium effect ($0.3 \leq r_{rb} < 0.5$), White = small effect ($r_{rb} < 0.3$). Raincloud plots show the distribution of the volumetric measures in each ROI per group with orange for HD and green for HC participants. * $p < 0.05$; *** $p < 0.001$

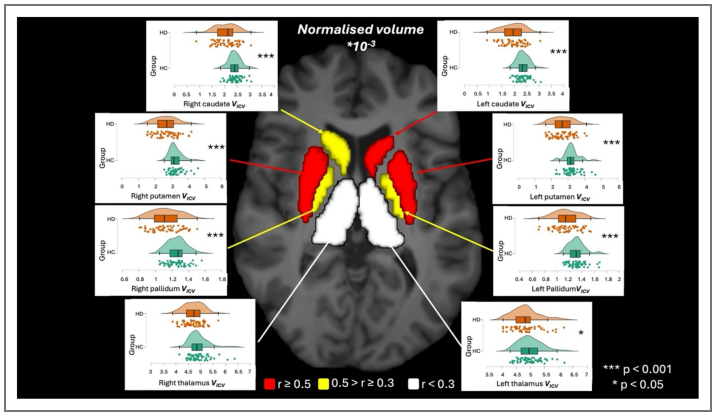

Table 2. **Descriptive and Mann-Whitney Statistics for Intracranial Volume-Normalised Regions of Interest**

		HD group	HC group	Statistic (FDR-p, effect size)
Region of interest	**L/R**	**Mean (SD)**	**Mean (SD)**	**U (p, rank-biserial correlation)**
Caudate	*L*	1.95[a] (0.45[a])	2.35[a] (0.24[a])	**2464 (<0.001, 0.544)**
	R	2.06[a] (0.43[a])	2.41[a] (0.25[a])	**2376 (<0.001, 0.489)**
Putamen	*L*	2.67[a] (0.62[a])	3.22[a] (0.46[a])	**2397 (<0.001, 0.502)**
	R	2.67[a] (0.66[a])	3.25[a] (0.40[a])	**2479 (<0.001, 0.553)**
Pallidum	*L*	1.15[a] (0.20[a])	1.32[a] (0.13[a])	**2382 (<0.001, 0.492)**
	R	1.13[a] (0.17[a])	1.26[a] (0.12[b])	**2323 (<0.001, 0.456)**
Thalamus	*L*	4.83[a] (0.49[a])	4.99[a] (0.41[b])	1955 (0.063, 0.224)
	R	4.72[a] (0.39[a])	4.91[a] (0.40[b])	**1981 (0.048, 0.241)**

Abbreviations: **FDR**: False Discovery Rate; **HC**: Healthy Controls; **HD**: Huntington's Disease; **L**: Left Hemisphere; **R**: Right Hemisphere; **SD**: Standard Deviation

[a]: Multiplied by 10^{-3}

Figure 2. **Microstructural differences in ROIs between HD and healthy control (HC) groups.**

Median values of each microstructural measure were extracted per ROI. **A)** HD individuals show reduced soma density (f_{is}) in the basal ganglia (BG). **B)** Soma radius (r_s) is elevated in the caudate and putamen but reduced in the pallidum. **C)** Extracellular water fraction (f_{ec}) is increased in BG regions in the HD group. **D)** Extracellular diffusivity (D_e) is higher in the putamen and pallidum. **E)** Fractional anisotropy (FA) is elevated in the BG, and **F)** mean diffusivity (MD; expressed in $x10^{-4}mm^2/s$) is increased in the striatum. Colours indicate the strength of rank-biserial correlations (r_{rb}) from Mann-Whitney U tests: Red = strong effect ($r_{rb} \geq 0.5$), Yellow = medium effect ($0.3 \leq r_{rb} < 0.5$), White = small effect ($r_{rb} < 0.3$). Raincloud plots show the distribution of the volumetric measures in each ROI per group with orange for HD and green for HC participants. * $p < 0.05$; ** $p < 0.01$; *** $p < 0.001$

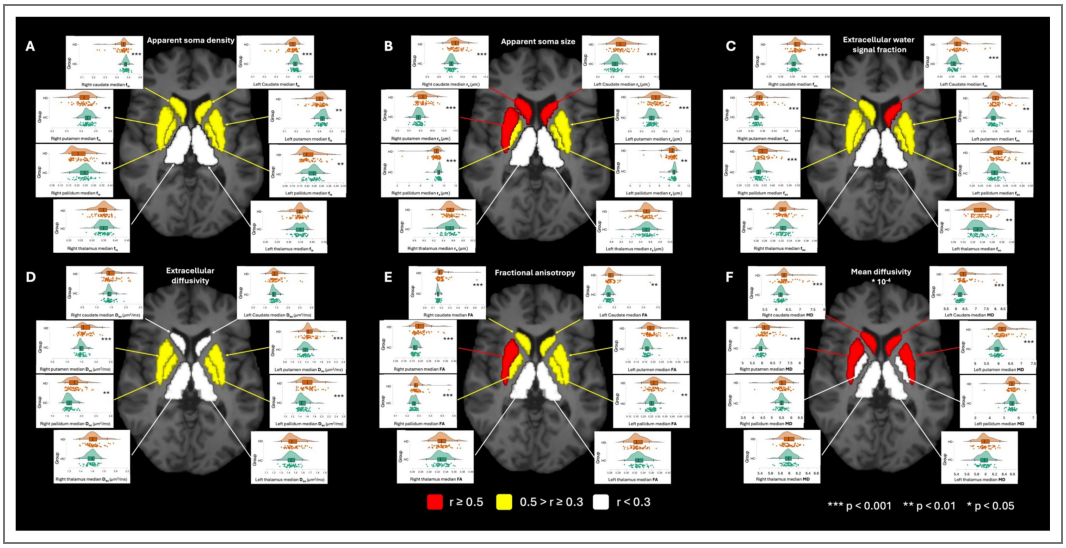

Table 3. Descriptive and Mann-Whitney Statistics for Microstructural Measures in Regions of Interest

			HD group	HC group	Statistic (FDR-p, effect size)
Microstructural measure	**Region of interest**	**L/R**	**Mean (SD)**	**Mean (SD)**	***U* (*p*, *rank-biserial correlation*)**
Apparent soma density	*Caudate*	*L*	0.43 (0.05)	0.46 (0.02)	**2227 (<0.001, 0.395)**
		R	0.45 (0.05)	0.48 (0.02)	**2318 (<0.001, 0.452)**
	Putamen	*L*	0.39 (0.05)	0.42 (0.03)	**2140 (0.003, 0.341)**
		R	0.42 (0.05)	0.44 (0.03)	**2099 (0.007, 0.315)**
	Pallidum	*L*	0.21 (0.05)	0.24 (0.04)	**2187 (0.001, 0.370)**
		R	0.21 (0.05)	0.24 (0.04)	**2249 (<0.001, 0.409)**
	Thalamus	*L*	0.34 (0.03)	0.34 (0.02)	1692 (0.701, 0.060)
		R	0.35 (0.03)	0.35 (0.02)	1661 (0.776, 0.041)
Apparent soma size	*Caudate*	*L*	9.80 (0.25)	9.58 (0.15)	**746 (<0.001, -0.533)**
		R	9.72 (0.25)	9.52 (0.12)	**751 (<0.001, -0.529)**
	Putamen	*L*	9.61 (0.29)	9.43 (0.15)	**885 (<0.001, -0.445)**
		R	9.63 (0.27)	9.40 (0.14)	**791 (<0.001, -0.504)**
	Pallidum	*L*	8.41 (1.08)	8.88 (0.58)	**2126 (0.004, 0.332)**
		R	8.59 (0.94)	9.05 (0.45)	**2300 (<0.001, 0.447)**
	Thalamus	*L*	9.51 (0.14)	9.50 (1.32)	1502 (0.701, -0.059)
		R	9.54 (0.13)	9.52 (0.12)	1515 (0.723, -0.051)
Extracellular signal fraction	*Caudate*	*L*	0.38 (0.04)	0.36 (0.01)	**757 (<0.001, -0.526)**
		R	0.37 (0.02)	0.36 (0.01)	**984 (<0.001, -0.383)**
	Putamen	*L*	0.36 (0.03)	0.34 (0.02)	**1048 (0.003, -0.343)**
		R	0.34 (0.03)	0.32 (0.01)	**892 (<0.001, -0.441)**
	Pallidum	*L*	0.36 (0.04)	0.33 (0.02)	**910 (<0.001, -0.430)**
		R	0.35 (0.04)	0.32 (0.02)	**932 (<0.001, -0.416)**
	Thalamus	*L*	0.34 (0.02)	0.33 (0.01)	1294 (0.130, -0.189)
		R	0.33 (0.01)	0.32 (0.01)	1636 (0.853, 0.025)
Extracellular diffusivity	*Caudate*	*L*	1.47 (0.28)	1.40 (0.11)	1420 (0.418, -0.110)
		R	1.51 (0.25)	1.44 (0.13)	1482 (0.633, -0.071)
	Putamen	*L*	1.47 (0.17)	1.36 (0.11)	**902 (<0.001, -0.435)**
		R	1.62 (0.20)	1.49 (0.11)	**1002 (0.001, -0.372)**
	Pallidum	*L*	1.62 (0.20)	1.48 (0.12)	**842 (<0.001, -0.472)**
		R	1.76 (0.23)	1.59 (0.14)	**809 (<0.001, -0.493)**
	Thalamus	*L*	1.47 (0.07)	1.44 (0.07)	1411 (0.394, -0.116)
		R	0.31 (0.03)	0.31 (0.03)	1377 (0.305, -0.137)
Apparent neurite density	*Caudate*	*L*	0.18 (0.04)	0.17 (0.02)	1514 (0.723, -0.051)
		R	0.18 (0.05)	0.16 (0.02)	1317 (0.167, -0.175)
	Putamen	*L*	0.24 (0.04)	0.23 (0.03)	1374 (0.303, -0.139)
		R	0.23 (0.04)	0.23 (0.03)	1411 (0.394, -0.116)
	Pallidum	*L*	0.41 (0.05)	0.42 (0.03)	1553 (0.854, -0.027)

		R	0.43 (0.05)	0.43 (0.03)	1473 (0.605, -0.078)
	Thalamus	*L*	0.31 (0.03)	0.31 (0.03)	1565 (0.868, -0.019)
		R	0.31 (0.03)	0.31 (0.03)	1459 (0.554, -0.086)
Fractional anisotropy	*Caudate*	*L*	0.18 (0.04)	0.16 (0.02)	**993 (0.001, -0.378)**
		R	0.20 (0.07)	0.16 (0.02)	**889 (<0.001, -0.443)**
	Putamen	*L*	0.19 (0.04)	0.17 (0.02)	**873 (<0.001, -0.453)**
		R	0.20 (0.04)	0.17 (0.02)	**710 (<0.001, -0.555)**
	Pallidum	*L*	0.28 (0.04)	0.26 (0.03)	**1115 (0.010, -0.301)**
		R	0.28 (0.05)	0.26 (0.02)	**995.5 (<0.001, -0.401)**
	Thalamus	*L*	0.33 (0.02)	0.33 (0.02)	1808 (0.319, 0.133)
		R	0.33 (0.02)	0.33 (0.02)	1532 (0.776, -0.040)
Mean diffusivity	*Caudate*	*L*	6.50^{a} (0.41^{a})	6.23^{a} (0.13^{a})	**777.5 (<0.001, -0.513)**
		R	6.44^{a} (0.36^{a})	6.20^{a} (0.12^{a})	**760.5 (<0.001, -0.523)**
	Putamen	*L*	6.22^{a} (0.34^{a})	5.95^{a} (0.15^{a})	**653.5 (<0.001, -0.591)**
		R	6.20^{a} (0.34^{a})	5.91^{a} (0.13^{a})	**624.5 (<0.001, -0.609)**
	Pallidum	*L*	5.54^{a} (0.36^{a})	5.51^{a} (0.23^{a})	1557.5 (0.854, -0.024)
		R	5.52^{a} (0.30^{a})	5.49^{a} (0.18^{a})	1437 (0.474, -0.100)
	Thalamus	*L*	5.98^{a} (0.14^{a})	5.96^{a} (0.11^{a})	1509 (0.721, -0.055)
		R	6.01^{a} (0.13^{a})	6.00^{a} (0.11^{a})	1566.5 (0.868, -0.018)

Abbreviations: **FDR**: False Discovery Rate; **HC**: Healthy Controls; **HD**: Huntington's Disease; **L**: Left Hemisphere; **R**: Right Hemisphere; **SD**: Standard Deviation

[a]: Multiplied by 10^{-4}

Table 3. (continued)

Spearman's rho correlations between Q-motor component scores and SANDI microstructural measures from all ROIs and scatter plots are displayed in Figure 3. Figure 4 displays correlations and scatter plots of the Q-Motor component with DTI and volumetric indices. Overall, negative correlations were observed between principal Q-Motor component scores and apparent soma density in the BG, apparent soma size in the pallidum, and volumetric measurements in all ROIs, indicating that lower apparent soma density and volumes were associated with impaired motor performance, reflected in higher scores in the Q-Motor component. Conversely, positive correlations were present between Q-Motor component scores and apparent soma size, extracellular signal fraction, and extracellular diffusivity in the BG, i.e. larger apparent soma size and extracellular signal were associated with impaired motor performance (Figure 3).

Microstructural predictors of BG volumes

Hierarchical linear regression analyses of the HC data (Table 4, Figure 5) revealed that 17% of volumetric variation in the left caudate was accounted for by age and apparent soma density while 11% of variation in the right caudate was explained by age and extracellular diffusivity (D_e). Age accounted for 25% of volumetric differences in the left putamen, and together with D_e for 29% of differences in right putamen. Age alone explained 17% of left and 11% of right thalamic volume variation. No significant regression models were present for bilateral globus pallidus.

In contrast, regression analyses for the HD data (Table 5, Figure 6) showed that 60% of volume variation in the left caudate and 51% of variation in the right caudate were accounted for by age and apparent soma density and size. Similarly, 57% of variation in the right putamen volume were explained by age and apparent soma size, while 63% of volume differences in the left putamen were explained by age, apparent soma size as well as extracellular signal and diffusivity. Comparable to the HC results, age alone accounted for 30% of volume variation in the left and for 35% in the right thalamus while no age effects were present for bilateral globus pallidus. However, in HD individuals 42% of volume variation in the left pallidum was explained by apparent soma size and extracellular signal and 27% of volume variation in the right pallidum by extracellular signal fraction only. No significant contributions of TFC were present.

Correlation of disease burden with microstructural and volumetric measures

The CAP_{100} score as an index of disease progression was correlated with brain measurements to explore the relationship between disease burden and microstructural and volumetric differences (Figure 7). Figure 7A summarises correlation coefficient strengths and levels of significance. Figures 7B-J display scatter plots of significant correlations between the CAP_{100} and microstructural and volumetric measures. Increased CAP_{100} was negatively correlated with apparent soma density, and volume size in bilateral caudate and putamen, as well as with pallidal apparent soma size. Positive correlations were observed between CAP_{100} and extracellular diffusivity and signal fraction, apparent soma size in caudate, putamen, and thalamus, apparent neurite density in putamen, FA in the BG, and MD in caudate and putamen.

Exploratory pairwise comparisons between HD-ISS groups and HC

Exploratory comparisons of apparent soma density, apparent soma size, extracellular signal fraction and extracellular diffusivity, averaged across left and right BG ROIs, were conducted between HD-ISS 0-1 (n = 13), HD-ISS 2-3 (n = 17), and HC (Supplementary Table 1).

Compared with HC, HD-ISS 0-1 showed increased extracellular signal fraction in the BG, larger apparent soma size in the caudate and putamen, and lower apparent soma density alongside larger extracellular diffusivity in the pallidum (r_{rb} = -0.255–0.483, $p \leq 0.033$). Relative to HD-ISS 0-1, those at HD-ISS 2-3 exhibited reduced apparent soma density and increased extracellular diffusivity in the caudate and putamen, as well as smaller apparent soma size in the pallidum (r_{rb} = -0.439–0.447, p = 0.01–0.031). Compared with HC, the HD-ISS 2-3 group showed differences in the

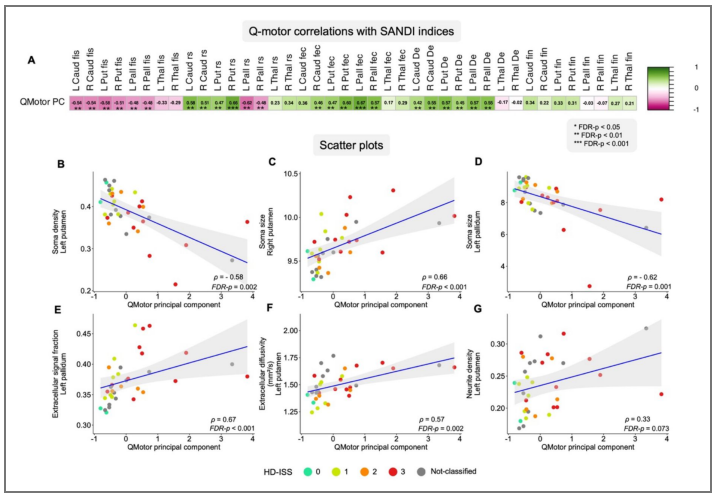

Figure 3.

A) Correlation matrix and **B-G)** selected scatter plots illustrating Spearman's rho correlations between SANDI measures and the Q-Motor principal component. **A)** Each cell represents the Spearman's rho correlation strength, with pink indicating negative and green positive correlations. **B-G)** Each plot includes a best-fit least squares linear regression line with standard error indicated by the grey shaded area, along with the Spearman's rho (ρ) and the corresponding FDR-p value. Regression lines are included for visualisation only and do not reflect variance explained (R^2) or imply linear model fit. Scatter dot colours represent participants' HD-ISS stage. Unclassified refers to those participants who could not be classified due to having CAG 36-40 or incomplete clinical data. **Abbreviations:** $\mathbf{D_e}$: Extracellular diffusivity; $\mathbf{f_{ec}}$: Extracellular signal fraction; $\mathbf{f_{in}}$: Neurite density signal fraction; $\mathbf{f_{is}}$: Soma density signal fraction; **PC**: Principal component; $\mathbf{r_s}$: Soma radius; **TFC**: Total functional capacity.

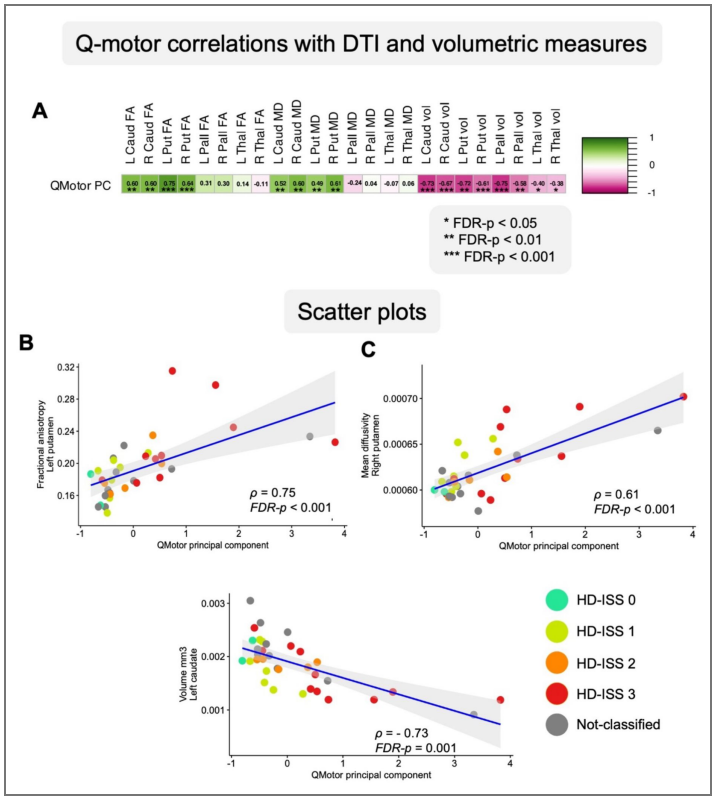

Figure 4.

A) Correlation matrix and **B-D)** selected scatter plots illustrating Spearman's rho correlations between DTI, volumetric measures and the Q-Motor principal component. **A)** Each cell represents the Spearman's rho correlation strength, with pink indicating negative and green positive correlations. **B-D)** Each plot includes a best-fit least squares linear regression line with standard error indicated by the grey shaded area, along with the Spearman's rho (ρ) and the corresponding FDR-p value. Regression lines are included for visualisation only and do not reflect variance explained (R^2) or imply linear model fit. Scatter dot colours represent participants' HD-ISS stage. Unclassified refers to those participants who could not be classified due to having CAG 36-40 or incomplete clinical data. **Abbreviations: FA**: Fractional anisotropy; **MD**: Mean diffusivity.

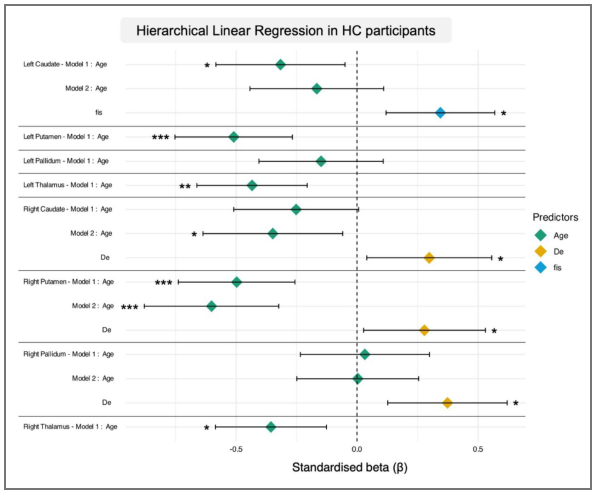

Figure 5. Standardised beta coefficients of SANDI microstructural metrics predicting volume (normalised for intracranial volume) in regions of interest in the healthy control group.

Data were modelled by firstly accounting for age, followed by the step-wise inclusion of all SANDI indices. The figure displays the predictor variables included in the final regression models for each region of interest. **Abbreviations: De**: Extracellular diffusivity; **fis**: Soma density signal fraction; **rs**: Soma radius; **TFC:** Total functional capacity. * $p < 0.05$; ** $p < 0.01$; *** $p < 0.001$.

Table 4. Hierarchical Linear Regression Predicting Normalised Volumes from SANDI Microstructural Metrics, Controlling for Age in the Healthy Control Participants

ROI	Model	Predictor(s)	*Adjusted R^2*	*ΔR^2*	*F-value (p-value)*	*ΔF-value*	*β*	*t-value*	*p-value*
Left Caudate	1	Age	0.084	0.100	**6.115 (0.017)**		-0.316	-2.473	**0.031**
	2	Age	0.167	0.096	**6.599 (0.003)**	6.474	-0.166	-1.226	0.297
		f_{is}					0.345	2.544	**0.026**
Left Putamen	1	Age	0.247	0.260	**19.328 (<0.001)**		-0.510	- 4.396	**<0.001**
Left Pallidum	1	Age	0.004	0.022	1.247 (0.269)		-0.149	-1.117	0.341
Left Thalamus	1	Age	0.174	0.188	**12.761 (0.001)**		-0.434	-3.572	**0.003**
Right Caudate	1	Age	0.046	0.063	3.715 (0.059)		-0.252	-1.927	0.087
	2	Age	0.111	0.080	**4.508 (0.015)**	5.029	-0.348	-2.616	**0.023**
		D_e					0.299	2.243	**0.048**
Right Putamen	1	Age	0.234	0.248	**18.109 (<0.001)**		-0.498	-4.255	**<0.001**
	2	Age	0.289	0.067	**12.389 (<0.001)**	5.265	-0.602	-4.954	**<0.001**
		De					0.279	2.295	**0.045**
Right Pallidum	1	Age	-0.017	0.001	.058 (0.811)		0.032	0.241	0.847
	2	Age	0.108	0.139	**4.392 (0.017)**	8.718	0.003	0.025	0.980
		D_e					0.374	2.953	**0.011**
Right Thalamus	1	Age	0.111	0.127	**7.966 (0.007)**		-0.356	-2.822	**0.015**

Model 1: Volume(ROI)=$\beta_0+\beta_1$*(Age) +ϵ; **Model 2-n**: Volume (ROI)=$\beta_0+\beta_1$*(Age)+ $\beta_{2\text{-}n}$*(f_{is}, r_s, f_{ec}, D_e, f_{in})+ϵ; Predictors in Model 1 were entered simultaneously; predictors in Models 2-n were entered in a stepwise fashion using an iterative forward selection and backward elimination method to maximise the adjusted R^2while keeping only the most significant predictors.

Abbreviations: De: Extracellular diffusivity; **fec:** Extracellular signal fraction; **fin:** Neurite density signal fraction; **fis:** Soma density signal fraction; **rs:** Soma size; **SANDI:** Soma And Neurite Density Imaging; **TFC:** Total Functional Capacity

Significant F-values and t-values are highlighted in **bold**

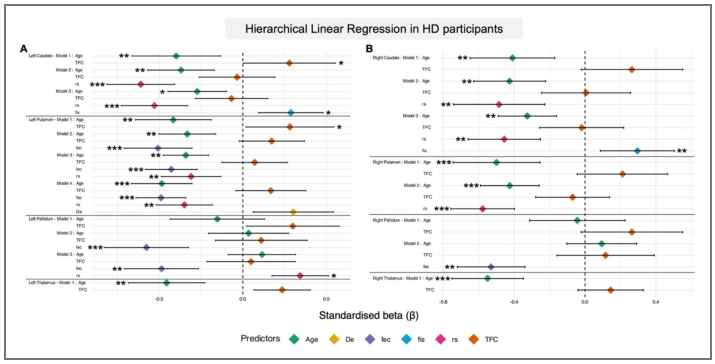

Figure 6. Standardised beta coefficients of SANDI microstructural metrics predicting volume (normalised for intracranial volume) in A) left and B) right hemisphere regions of interest in individuals with Huntington's disease.

Data were modelled by firstly accounting for age and Total Functional Capacity scores simultaneously, followed by the step-wise inclusion of all SANDI indices. The figure displays the predictor variables included in the final regression models for each region of interest. **Abbreviations: De**: Extracellular diffusivity; **fec**: Extracellular signal fraction; **fis**: Soma density signal fraction; **rs**: Soma radius. * $p < 0.05$; ** $p < 0.01$; *** $p < 0.001$.

ROI	Model	Predictors	*Adjusted R^2*	*ΔR^2*	*F-value (p-value)*	*ΔF-value*	*β*	*t-value*	*p-value*
Left Caudate	1	Age	0.277	0.304	**11.136 (<0.001)**		-0.398	-3.249	**0.005**
		TFC					0.280	2.281	**0.046**
	2	Age	0.547	0.268	**22.308 (<0.001)**	31.383	-0.370	-3.810	**<0.001**
		TFC					-0.034	-0.303	0.822
		r_s					-0.611	-5.602	**<0.001**
	3	Age	0.600	0.058	**20.853 (<0.001)**	7.623	-0.273	-2.788	**0.016**
		TFC					-0.068	-0.638	0.594
		r_s					-0.529	-4.963	**<0.001**
		f_{is}					0.288	2.761	**0.016**
Left Putamen	1	Age	0.296	0.323	**12.150 (<0.001)**		-0.415	-3.436	**0.003**
		TFC					0.282	2.331	**0.043**
	2	Age	0.529	0.233	**20.855 (<0.001)**	26.238	-0.332	-3.311	**0.005**
		TFC					0.173	1.711	0.129
		f_{ec}					-0.507	-5.122	**<0.001**
	3	Age	0.601	0.075	**20.934 (<0.001)**	9.961	-0.341	-3.690	**0.003**
		TFC					0.071	0.721	0.552
		f_{ec}					-0.427	-4.515	**<0.001**
		r_s					-0.309	-3.156	**0.007**
	4	Age	0.630	0.034	**19.016 (<0.001)**	4.818	-0.485	-4.386	**<0.001**
		TFC					0.168	1.605	0.157
		f_{ec}					-0.489	-5.126	**<0.001**
		r_s					-0.349	-3.638	**0.003**
		D_e					0.302	2.195	0.052
Left Pallidum	1	Age	0.107	0.140	**4.165 (0.021)**		-0.152	-1.119	0.341
		TFC					0.299	2.198	0.052

Table 5. Hierarchical Linear Regression Models Predicting Normalised Volumes in each Region of Interest from SANDI Microstructural Metrics, Controlling for Age and TFC in HD Participants

Table 5. (continued)

	2	Age	0.344	0.241	**10.278 (<0.001)**	19.485	0.035	0.278	0.829
		TFC					0.111	0.889	0.455
		f_{ec}					-0.577	-4.414	**<0.001**
	3	Age	0.424	0.086	**10.741 (<0.001)**	7.885	0.115	0.961	0.425
		TFC					0.049	0.417	0.753
		f_{ec}					-0.486	-3.837	**0.001**
		r_s					0.344	2.808	**0.015**
Left Thalamus	1	Age	0.302	0.328	**12.455 (<0.001)**		-0.456	-3.786	**0.001**
		TFC					0.236	1.956	0.085
Right Caudate	1	Age	0.276	0.304	**11.117 (<0.001)**		-0.410	-3.341	**0.005**
		TFC					0.265	2.162	0.054
	2	Age	0.443	0.171	**15.036 (<0.001)**	16.233	-0.426	-3.957	**0.001**
		TFC					0.006	0.048	0.976
		r_s					-0.485	-4.029	**0.001**
	3	Age	0.510	0.073	**14.807 (<0.001)**	7.898	-0.326	-3.043	**0.009**
		TFC					-0.018	-0.156	0.902
		r_s					-0.456	-4.020	**0.001**
		f_{is}					0.296	2.810	**0.015**
Right Putamen	1	Age	0.333	0.358	**14.218 (<0.001)**		-0.499	-4.243	**<0.001**
		TFC					0.211	1.797	0.111
	2	Age	0.570	0.236	**24.432 (<0.001)**	29.159	-0.425	-4.450	**<0.001**
		TFC					-0.070	-0.652	0.593
		rs					-0.578	-5.400	**<0.001**
Right Pallidum	1	Age	0.043	0.079	2.177 (0.124)		-0.043	-0.308	0.822
		TFC					0.264	1.874	0.097
	2	Age	0.265	0.228	**7.367 (<0.001)**	16.430	0.094	0.737	0.550
		TFC					0.116	0.902	0.454
		f_{ec}					-0.530	-4.053	**0.001**
Right Thalamus	1	Age	0.347	0.372	**15.076 (<0.001)**		-0.550	-4.723	**<0.001**
		TFC					0.145	1.242	0.295

Model 1: Volume(ROI)=$\beta_0+\beta_1$*(Age)+β_2*(TFC) +ϵ; **Model 2-n**: Volume (ROI)=$\beta_0+\beta_1$*(Age)+β_2*(TFC)+β_{3-n}*(f_{is}, r_s, f_{ec}, D_e, f_{in})+ϵ; Predictors in Model 1 were entered simultaneously; predictors in Models 2-n were entered in a stepwise fashion using an iterative forward selection and backward elimination method to maximise the adjusted R^2while keeping only the most significant predictors.

Abbreviations: De: Extracellular diffusivity; **fec:** Extracellular signal Fraction; **fin:** Neurite density signal fraction; **fis:** Soma density signal fraction; **HD:** Huntington's Disease; **rs:** Soma size; **SANDI:** Soma And Neurite Density Imaging; **TFC:** Total Functional Capacity

Significant F-values and t-values ($p<0.05$) are highlighted in **bold**

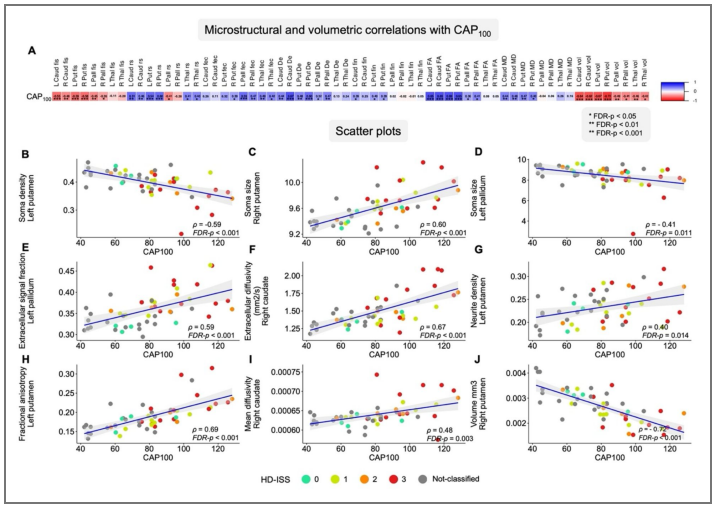

Figure 7.

A) Correlation matrix and **B-J)** selected scatter plots illustrating Spearman's rho correlations between SANDI, DTI, and volumetric measures with CAP_{100}. Each scatter plot includes a best-fit least squares linear regression line with standard error indicated by the grey shaded area, along with the Spearman's rho (ρ) and the corresponding FDR-p value. Regression lines are included for visualisation only and do not reflect variance explained (R^2) or imply linear model fit. Scatter dot colours represent participants' HD-ISS stage and those who were not classified due to having CAG<40 or incomplete clinical data. **Abbreviations: De**: Extracellular diffusivity; **FA**: Fractional anisotropy; **fec**: Extracellular signal fraction; **fin**: Neurite density signal fraction; **fis**: Soma density signal fraction; **MD**: Mean diffusivity; **rs**: Soma radius; **vol**: Normalised volume.

same directions across all metrics in all BG regions. Descriptive statistics and full statistical analysis results are provided in Supplementary Table 4, and effect sizes with 95% confidence intervals are shown in Supplementary Figure 2.

Cross-correlations between microstructural and volumetric measures

Cross-correlation matrices between SANDI microstructural indices, DTI metrics, and normalised volumes are shown in Supplementary Figure 3 for the full sample, and separately for HC and HD groups. Across all participants, moderate to strong correlations were observed between conceptually related diffusion-derived measures (e.g. mean diffusivity with extracellular diffusivity, fractional anisotropy with neurite-related indices), indicating partially shared variance as expected. In the HC group, SANDI metrics reflecting apparent soma properties (soma radius and soma fraction) showed distinct correlation patterns: soma and neurite fraction were strongly inversely correlated (ρ = -0.92) but neither correlated with soma radius. All SANDI measures correlated weakly with FA and volume and moderately with MD. Group-specific matrices revealed broadly similar correlation structures in HC and HD participants. However, several associations, particularly between SANDI indices and normalised volume, were stronger in the HD group, consistent with disease-related coupling between microstructural alterations and macroscopic atrophy.

Discussion

This study is the first to investigate HD-related microstructural differences in the BG using SANDI, a diffusion MRI technique designed to probe grey matter microstructure. The objective of the study was to explore SANDI indices as potential non-invasive *in vivo* markers of HD neuropathology that may offer greater specificity than volumetric measurements. Apparent soma density and apparent soma size were sensitive to HD-related differences in the BG and together with age, accounted for up to 63% of striatal atrophy. SANDI indices also correlated with motor impairments and CAP_{100} disease burden. Together, these findings highlight the potential of SANDI metrics as imaging biomarkers of disease progression and as surrogate outcome measures for assessing the neural effects of emerging disease-modifying therapies in HD and other neurodegenerative diseases.

Microstructural and Volumetric Alterations in HD

Well-established patterns of marked volume loss accompanied by increases in FA and MD in the BG were replicated in HD compared with healthy controls. FA increases in the caudate and putamen are thought to reflect the selective degeneration of MSN connections.[20,84] No microstructural differences and only trends for volumetric reduction were observed in the thalami. This pattern of macro- and microstructural differences in the BG aligns with previous reports in premanifest and early manifest HD stages.[31,85]

Importantly, SANDI revealed novel HD-related microstructural differences in the BG. Compared with healthy controls, those with HD showed reduced apparent soma density together with increased extracellular signal fraction and diffusivity across the caudate, putamen, and pallidum, but not the thalami. Apparent soma size was also increased in the caudate and putamen, whereas it was reduced in the globus pallidus.

HD-related reductions in apparent soma density in the BG are consistent with the loss of striatal MSN, the histopathological hallmark of HD,[22,23] and with downstream degeneration of pallidal neurons by the loss of striatal projections. Changes in apparent soma size may reflect alterations in neural and glial cell proportions and/or morphology, including astrocyte and microglia swelling in response to neurodegeneration[22,24–26] as well as soma shrinkage preceding neuronal cell death.[86,87] Thus, increased apparent soma size in the striatum may indicate HD-related

reorganisation of cell composition driven by MSN loss and reactive glial cell swelling, whereas smaller apparent soma size in the pallidum may reflect infiltration of smaller glia cells associated with secondary neuronal loss following striatal degeneration.

Exploratory analyses of BG SANDI differences across HD-ISS Stages 0-3 (Supplementary Figure 2) showed that reductions in striatal apparent soma density and increases in extracellular diffusivity were evident in HD-ISS 2-3 but not in HD-ISS 0-1, whereas increases in striatal apparent soma size and extracellular signal fraction were present in both groups. In the pallidum, reductions in apparent soma density and increases in extracellular signal fraction and diffusivity were observed in both HD-ISS groups, while reduced apparent soma size was only present in HD-ISS 2-3. These findings suggest that SANDI indices are sensitive to changes in BG cellular composition both at early (HD-ISS 0-1) and across disease stages (HD-ISS 0-3). However, these preliminary observations require validation in larger, prospective cohorts before SANDI indices can be considered reliable biomarker of disease progression.

With the development of disease-modifying therapies for HD, the need for non-invasive imaging markers that can sensitively capture treatment effects has become increasingly important. Striatal volume remains the gold-standard imaging marker, and DTI has been widely used to assess tissue microstructure in both cross-sectional and longitudinal studies.[2,13–15,88] An important question therefore concerns how SANDI indices compare with these established imaging markers and the extent to which they share variance.

In this study we observed moderate effect sizes for group differences in striatal SANDI indices, comparable to those for volume, FA, and MD. ES for apparent soma size overlapped with those for volume and MD, while apparent soma density showed slightly lower but broadly similar ES to FA.

Multicollinearity between microstructural and volumetric imaging measures was assessed using cross-correlations between all imaging metrics (SANDI, DTI, volume) averaged across ROIs (see Supplementary Figure 2). In HCs, apparent soma and neurite fractions were strongly inversely correlated but neither correlated with soma radius. SANDI indices showed only weak correlations with FA and volume, but moderate correlations with MD. This pattern suggests that soma density and size parameters capture microstructural features that are distinct from neurite fraction, FA, and volume, but overlap to some extent with MD, an unspecific metric influenced by multiple biological and geometrical tissue properties.[89,90] In HD participants, correlations between SANDI metrics and volumes were stronger, and soma radius and fraction were inversely correlated, likely reflecting disease-related reorganisation of microstructural properties associated with atrophy.

Microstructural predictors of basal ganglia atrophy in HD

To explore the relationship between SANDI microstructural and volumetric measures in the BG, hierarchical linear regression analyses were conducted for each ROI and for HD and HC groups separately, testing age and SANDI indices as predictors of volume. For the HD group, TFC was included as a marker of disease burden. These analyses showed that SANDI indices accounted for a substantial proportion of BG atrophy but not thalamic volume.

Up to 63% of HD-related striatal atrophy was explained by apparent soma density, apparent soma size, and age. In the pallidum, apparent soma size and extracellular signal fraction accounted for 27% of atrophy on the right and 42% on the left, whereas age alone predicted thalamic volume. This pattern in the thalami mirrored findings in healthy controls, where age was the strongest predictor across all ROIs (except bilateral pallidum) and the only significant predictor in the thalami; diffusivity contributed to right-lateralised BG regions and apparent soma density to the left caudate.

Together, these results demonstrate that SANDI-derived measures of apparent soma density and size capture HD-related differences in striatal grey-matter microstructure *in vivo*. As outlined above, reductions in apparent soma density and increases in apparent soma size are consistent with the characteristic loss of medium spiny neurons and reactive gliosis in HD and explain a significant proportion of atrophy in the caudate and putamen.

Associations Between SANDI microstructural indices and Motor Function

The observed correlations between SANDI metrics and motor measures provide novel insights into the functional implications of microstructural alterations in HD. Consistent with the role of the BG in motor initiation and coordination,[91] the present study showed that reduced apparent soma density in the striatum and reduced apparent soma size in the pallidum were associated with poorer Q-Motor performance, which itself was linked to greater disease burden. This was reflected in increased IOI and ACU during speeded tapping tasks, and in impaired performance on paced tapping tasks. Similarly, increased apparent soma size in the striatum, together with elevated extracellular signal and diffusivity across all BG regions, as well as striatal FA and MD, were associated with motor impairments. These findings indicate that microstructural changes related to BG neurodegeneration and glial reactivity are directly linked to subtle motor deficits in HD.

Limitations

HD-ISS classification was possible for only 30 of the 56 HD participants (54%) due to the retrospective pooling of MRI datasets collected before HD-ISS information was incorporated into the Enroll-HD database, missing clinical data, and HD-ISS model exclusions for individuals with CAG repeat lengths between 36-39. Of the 30 classified participants, 4 were assigned to i Stage 0, 9 to Stage 1, 5 ito Stage 2, and 12 to Stage 3; none were classified as Stage 4. Because of the small sample sizes, HD-ISS comparisons were conducted on combined groups (HD-ISS 0-1 versus HD-ISS 2-3). These combined groups showed some overlap in imaging and behavioural features (Figures 3, 4, and 7) and therefore do not represent discrete disease stages. Consequently, these exploratory findings should be interpreted with caution and require replication in larger, prospective cohorts before SANDI metrics can be considered markers of disease progression.

In addition, several methodological considerations regarding HD-ISS classification should be noted. Classification was obtained either from Enroll-HD or calculated using the online HD-ISS tool. For participants labelled “<2” in Enroll-HD, Stages 0 and 1 were assigned based on z-scores for striatal volumes derived from the FreeSurfer v6 cross-sectional pipeline. However, HD-ISS classification and online calculator were developed using volume cut-offs generated from the longitudinal FreeSurfer v6 pipeline. Consequently, applying cross-sectional data in this study may have introduced classification bias.

Furthermore, hierarchical regression models were fitted separately within HD and HC groups and were not intended to support formal statistical comparisons of regression coefficients across groups. Rather, these analyses were designed to explore within-group associations and to provide a descriptive comparison of patterns of relationships linking microstructural indices to regional atrophy. Hierarchical regression models may also be susceptible to over-fitting, and therefore the reported coefficients may not reflect true out-of-sample R^2.

The assessment of potential multicollinearity between SANDI-derived metrics was based primarily on the healthy control data, as correlations observed in the HD group likely reflect disease-related shifts in microstructural relationships rather than intrinsic model dependencies. In healthy controls, soma radius did not correlate with apparent soma or neurite fractions, whereas a pronounced inverse relationship was observed between soma and neurite fractions, consistent with the biophysical constraints of the model. Importantly, correlations between SANDI metrics and conventional DTI measures (FA) and regional volume were generally weak, indicating that apparent soma estimates capture distinct aspects of grey matter microstructure rather than redundant information.

Moderate correlations with mean diffusivity were observed and are expected, given that MD is a non-specific metric sensitive to multiple microstructural features and susceptible to partial volume effects associated with tissue loss. Consequently, individual regression coefficients should not be interpreted in isolation as fully independent biological effects. As with all model-based approaches applied to correlated imaging parameters, some degree of shared variance and

parameter coupling is unavoidable. As we cannot rule out some degeneracy between apparent soma density f_{is} and apparent soma size r_s, r_s should not be interpreted as absolute histological soma radii, and inferences should instead focus on relative group differences and spatial patterns. Similarly, HD-related microstructural changes (e.g., changes to membrane permeability) could affect model parameter fidelity, and thus f_{is} and r_s should be treated as MRI-derived effective indices rather than direct quantitative measures of neuron loss or glial hypertrophy.

However, the correlation structure observed in healthy controls suggests that multicollinearity is unlikely to critically undermine model stability or interpretability in the present analyses. Importantly, all comparisons were made under an identical acquisition protocol and fitting pipeline, meaning that group-level contrasts remain informative even if absolute parameter values are biased. The primary conclusions of the present study therefore do not rely on the precise magnitude of individual coefficients but on the consistent pattern and direction of associations across regions and measures. Together, these factors support the feasibility and initial clinical relevance of SANDI for probing striatal microstructural alterations in Huntington's disease.

Clinical Implications and Future Directions

The present study acquired multi-shell (max b-value = 6,000 s/mm^2) DWI data on a non-clinical ultra-strong gradient (300mT/m) 3T MRI system. Ultra-strong gradients improve the signal-to-noise-ratio at high b-values by enabling shorter echo times (TE), thereby enhancing sensitivity to small water displacement,[39] and reducing bias from inter-compartmental exchange.[92,93]

However, for clinical translation it is important to demonstrate that HD-related SANDI differences can be detected on standard clinical MRI systems without requiring ultra-strong gradients. Although equivalent data in HD are not yet available, we have shown the feasibility of estimating SANDI metrics from multi-shell DWI acquired on a 3T MRI system with standard gradient strength (67mT/m) (maximum b-value of 6,000 s/mm^2) in healthy adults [94] and people with MS[42,44,94]. Additionally, Zeng et al.,[43] reported significant differences in SANDI metrics between individuals with ALS and healthy controls using a 3T MRI Prisma system with a maximum b-value of 3,000 s/mm^2, and two further studies using 3T clinical scanners with standard gradient strength showed detectable microstructural SANDI alterations in MS. Collectively, these findings indicate that SANDI can be implemented on clinical scanners, particularly as commercial systems progress toward stronger gradient capabilities such as Siemens Magnetom Cima.X.

Our findings highlight the potential of SANDI-derived metrics as future markers for tracking disease progression and assessing therapeutic efficacy in HD, as well as in more prevalent neurodegenerative conditions such as Alzheimer's and Parkinson's disease. The sensitivity of apparent soma density and size, and extracellular water signal to microstructural changes in HD provides information complementary to volumetric measures, which are currently the most widely used imaging modality in clinical trials. Furthermore, the observed associations between SANDI metrics, motor performance, and disease burden underscore their relevance for evaluating the neural effects of emerging disease-modifying treatments.

Ultimately, the choice of imaging markers depends on scientific or clinical objective: DTI and volumetric measures are informative for documenting differences or tracking longitudinal change, whereas gaining mechanistic insight into tissue microstructure and therapeutic effects requires going beyond DTI and volumes. Advanced models such as SANDI offer the potential to provide more specific and biologically meaningful characterisation of grey matter pathology.

Conclusion

Our study demonstrates the potential of SANDI for characterising microstructural abnormalities in individuals with HD. These abnormalities align with *ex vivo* neuropathological findings of striatal medium spiny neuron loss and gliosis, account for a substantial proportion of striatal atrophy, and correlate with motor impairment and disease burden. Although conventional MRI lacks the resolution to directly capture histopathology, advanced biophysical models such as SANDI may

help bridge this gap by providing biologically interpretable parameters that reflect tissue composition and capture histopathological changes *in vivo*. This approach offers a promising avenue for advancing HD research and improving clinical care.

Supplementary information

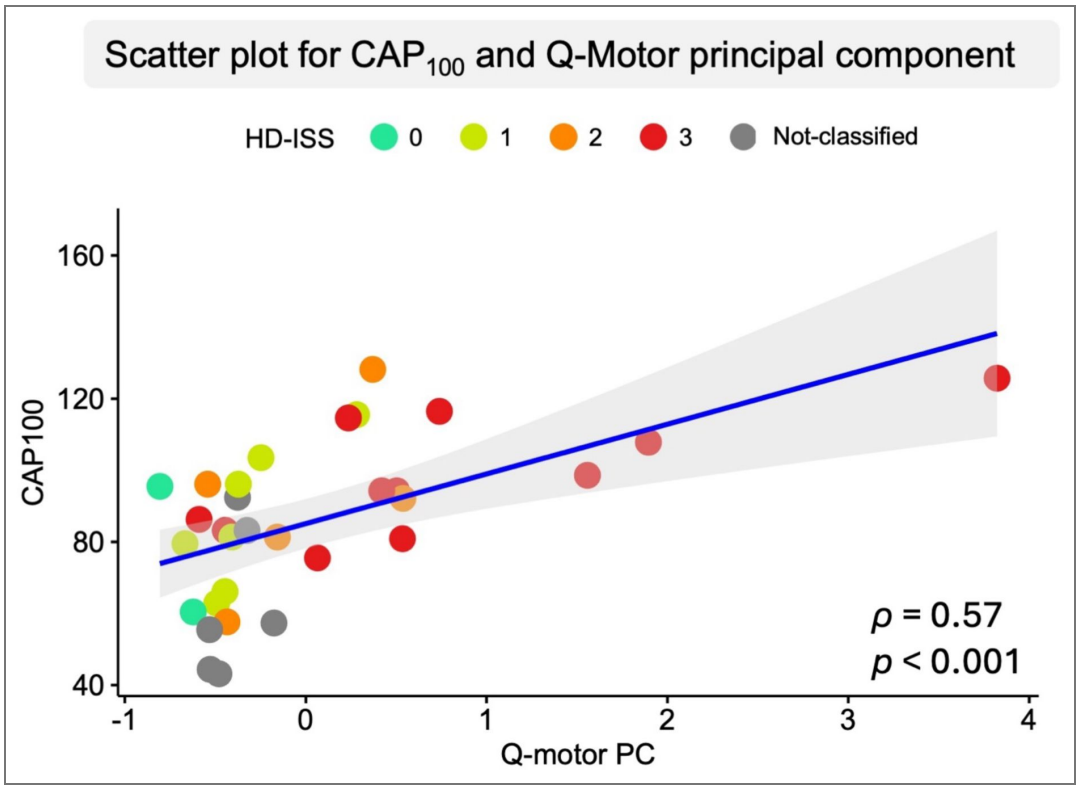

Supplementary Figure 1. Scatterplot showing positive relationship between the Q-Motor principal component and the disease burden measure (CAP_{100}) with the Spearman's rho (ρ) test. Scatter dot colours represent participants' HD-ISS stage and those who were not classified due to having CAG<40 or incomplete clinical data.

Supplementary Figure 2. Bar plot showing the effect sizes and 95% confidence intervals for exploratory pairwise comparisons between HD-ISS 0-1 (n = 13), HD-ISS 2-3 (n = 17), and healthy controls (HC).

Significant comparisons are marked with * (p < 0.05), ** (p < 0.01), and *** (p < 0.001).

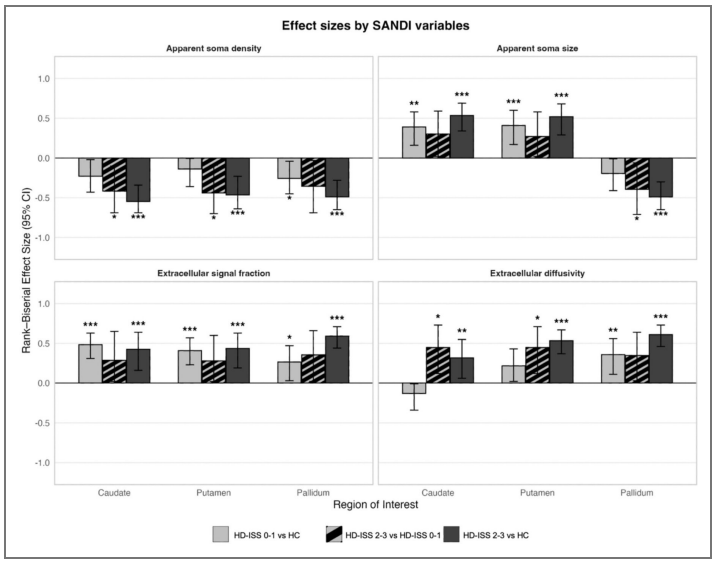

Supplementary Figure 3. Correlation heatmaps showing the cross-correlation of SANDI, DTI, and volumetric (normalised for intracranial volume) measures, averaged across the caudate, putamen, pallidum, and thalamus.

Heatmaps are shown separately for the full sample, healthy controls (HC), and Huntington's disease (HD) participants. Correlations are expressed as Spearman's rho coefficients.

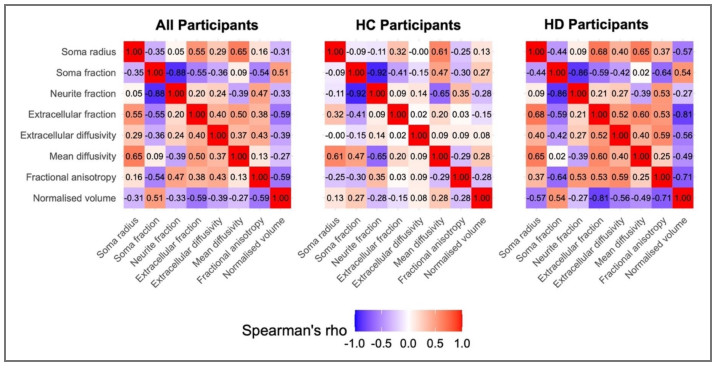

Supplementary Table 1. Demographic and clinical information per HD-ISS stage

	HD-ISS 0		HD-ISS 1		HD-ISS 2		HD-ISS 3		HD-ISS NA	
Measure	**N**	**Mean (SD)**	**N**	**Mean (SD)**	**N**	**Mean (SD)**	**N**	**Mean (SD)**	**N**	**Mean (SD)**
Age	4	37.75 (16.30)	9	47.11 (12.36)	5	48.80 (10.83)	12	49.17 (12.20)	26	42.65 (14.97)
Sex, Female (%)	4	3 (75%)	9	5 (56%)	5	1 (20%)	12	3 (25%)	26	13 (50%)
Education (years)	2	15.50 (0.71)	7	15.71 (1.38)	5	14.60 (3.71)	12	13.00 (2.17)	12	14.00 (3.13)
MOCA	4	25.50 (1.91)	9	28.00 (1.87)	5	26.00 (2.45)	11	23.73 (3.20)	26	27.35 (3.94)
TOPF	4	60.25 (5.38)	9	50.22 (14.03)	5	44.20 (14.10)	12	43.25 (10.34)	26	51.92 (13.67)
UHDRS-TFC	4	13.00 (0.00)	9	12.78 (0.44)	5	13.00 (0.00)	12	10.92 (1.16)	24	12.12 (1.30)
UHDRS-TMS	4	1.50 (3.00)	9	4.67 (4.90)	5	10.20 (1.48)	12	29.33 (20.38)	18	6.22 (11.34)
CAG	4	43.00 (2.16)	9	41.89 (1.17)	5	42.00 (1.00)	12	43.67 (3.14)	20	40.40 (2.56)
CAP100	4	72.34 (15.89)	9	85.50 (16.98)	5	91.09 (25.58)	12	99.70 (16.68)	20	65.84 (18.50)
SDMT	2	69.00 (5.66)	7	54.29 (13.03)	5	45.60 (8.73)	12	33.83 (12.65)	12	48.00 (12.62)

Abbreviations: **CAG**: Cytosine Adenine Guanine; **CAP**: CAG-Age-Product; **HC**: Healthy controls; **HD**: Huntington's disease; **HD-ISS**: HD-Integrated Staging System; **MOCA**: Montreal Cognitive Assessment; **SD**: Standard deviation; **SDMT**: Symbol Digit Modalities Task; **TFC**: Total Functional Capacity; **TMS**: Total Motor Score; **TOPF**: Test of Premorbid Functioning; **UHDRS**: United Huntington's Disease Rating Scale

Supplementary Table 2. Descriptive statistics for motor outcome measures

	HD group	
Task *Outcome measure*	**N**	**Mean (SD)**
Speeded tapping		
Left finger; Area under the curve (N-s)	38	0.13 (0.20)
Right finger; Area under the curve (N-s)	38	0.07 (0.09)
Left finger; Inter-onset interval (s)	38	0.26 (0.12)
Right finger; Inter-onset interval (s)	38	0.23 (0.08)
Left foot; Inter-onset interval (s)	37	0.37 (0.20)
Right foot; Inter-onset interval (s)	38	0.35 (0.18)
Metronome tapping; Absolute deviation from pace (s)		
Left finger; Paced; Fast	38	0.07 (0.06)
Left finger; Paced; Slow	38	0.13 (0.14)
Left finger; Unpaced; Fast	38	0.07 (0.07)
Left finger; Unpaced; Slow	38	0.15 (0.15)
Right finger; Paced; Fast	38	0.07 (0.06)
Right finger; Paced; Slow	38	0.13 (0.12)
Right finger; Unpaced; Fast	38	0.08 (0.06)
Right finger; Unpaced; Slow	38	0.16 (0.17)
Left foot; Paced; Fast	36	0.07 (0.05)
Left foot; Paced; Slow	35	0.16 (0.13)
Left foot; Unpaced; Fast	36	0.08 (0.09)
Left foot; Unpaced; Slow	35	0.17 (0.14)
Right foot; Paced; Fast	37	0.08 (0.04)
Right foot; Paced; Slow	37	0.16 (0.12)
Right foot; Unpaced; Fast	37	0.09 (0.09)
Right foot; Unpaced; Slow	37	0.16 (0.13)
Pointing (dominant hand)		
Target frequency over trial (Hz)	38	2.62 (0.65)
Pointing (dominant) and tapping (non-dominant)		
Finger tapping area under the curve (coefficient of variation %)	38	0.76 (0.37)
Finger tapping area under the curve (N-s)	38	0.31 (0.43)
Finger tapping inter-onset interval (s)	38	0.39 (0.19)
Frequency over trial (Hz)	38	3.08 (1.07)
Pointing target frequency over trial (Hz)	38	2.62 (0.66)

Abbreviations: Hz: Hertz; **N:** Newton; **s:** Seconds

Supplementary Table 3. Rotated Component Loadings on the Q-motor Outcome Measures

Task *Outcome measure*	**Q-motor Factor**
Speeded tapping	
Left finger; Area under the curve (N-s)	**0.707**
Right finger; Area under the curve (N-s)	**0.723**
Left finger; Inter-onset interval (s)	**0.772**
Right finger; Inter-onset interval (s)	**0.859**
Left foot; Inter-onset interval (s)	**0.798**
Right foot; Inter-onset interval (s)	**0.893**
Metronome tapping; Absolute deviation from pace (s)	
Left finger; Paced; Fast	**0.875**
Left finger; Paced; Slow	**0.832**
Left finger; Unpaced; Fast	**0.936**
Left finger; Unpaced; Slow	**0.913**
Right finger; Paced; Fast	**0.730**
Right finger; Paced; Slow	**0.672**
Right finger; Unpaced; Fast	**0.886**
Right finger; Unpaced; Slow	**0.865**
Left foot; Paced; Fast	**0.823**
Left foot; Paced; Slow	**0.883**
Left foot; Unpaced; Fast	**0.884**
Left foot; Unpaced; Slow	**0.900**
Right foot; Paced; Fast	**0.818**
Right foot; Paced; Slow	**0.885**
Right foot; Unpaced; Fast	**0.890**
Right foot; Unpaced; Slow	**0.740**
Pointing (dominant hand)	
Target frequency over trial (Hz)	**-0.525**
Pointing (dominant) and tapping (non-dominant)	
Finger tapping area under the curve (N-s)	**0.734**
Finger tapping inter-onset interval (s)	**0.788**
Frequency over trial (Hz)	**-0.756**
Pointing target frequency over trial (Hz)	**-0.568**

All loadings were significant (>0.5 and < -0.5) and are highlighted in bold.

Abbreviations: Hz: Hertz; **N:** Newton; **s:** Seconds

		Descriptive statistics Mean (SD)			Pairwise comparisons Statistic, (p-value) Effect size [CI 95%]		
Microstructural variable	**Region of interest**	**HD-ISS 0-1 N=13**	**HD-ISS 2-3 N=17**	**HC N=57**	**HD-ISS 0-1 vs HC**	**HD-ISS 2-3 vs HD-ISS 0-1**	**HD-ISS 2-3 vs HC**
Apparent soma density	Caudate	0.45 (0.02)	0.41 (0.07)	0.47 (0.02)	244 (0.057) -0.228 [-0.43 – -0.02]	**56 (0.024)** **-0.416 [-0.70 – -0.10]**	**119 (<0.001)** **-0.546 [-0.69 – -0.38]**
	Putamen	0.42 (0.03)	0.38 (0.05)	0.43 (0.03)	294 (0.251) -0.138 [-0.35 – -0.01]	**53 (0.017)** **-0.439 [-0.70 – -0.10]**	**174 (<0.001)** **-0.464 [-0.64 – -0.25]**
	Pallidum	0.22 (0.03)	0.19 (0.03)	0.24 (0.04)	**229 (0.033)** **-0.255 [-0.45 – -0.04]**	64 (0.054) -0.355 [-0.69 – -0.03]	**158 (<0.001)** **-0.488 [-0.65 – -0.30]**
Apparent soma size	Caudate	9.72 (0.17)	9.88 (0.28)	9.55 (0.13)	**587 (0.001)** **0.391 [0.14 – 0.57]**	150 (0.103) 0.302 [0.02 – 0.62]	**842 (<0.001)** **0.534 [0.32 – 0.69]**
	Putamen	9.62 (0.19)	9.77 (0.30)	9.41 (0.14)	**597 (<0.001)** **0.409 [0.19 – 0.60]**	146 (0.143) 0.271 [0.02 – 0.60]	**832 (<0.001)** **0.519 [0.27 – 0.68]**
	Pallidum	8.79 (0.52)	8.11 (1.44)	8.96 (0.51)	263 (0.106) -0.194 [-0.39 – -0.01]	**59 (0.033)** **-0.394 [-0.69 – -0.06]**	**157 (<0.001)** **-0.489 [-0.66 – -0.31]**
Extracellular signal fraction	Caudate	0.37 (0.01)	0.38 (0.03)	0.36 (0.01)	**638 (<0.001)** **0.483 [0.31 – 0.62]**	148 (0.121) 0.287 [0.02 – 0.64]	**769 (<0.001)** **0.425 [0.16 – 0.63]**
	Putamen	0.35 (0.01)	0.37 (0.04)	0.33 (0.01)	**597 (<0.001)** **0.409 [0.22 – 0.56]**	147 (0.132) 0.279 [0.02 – 0.62]	**776 (<0.001)** **0.435 [0.17 – 0.64]**
	Pallidum	0.35 (0.04)	0.38 (0.04)	0.33 (0.02)	**517 (0.027)** **0.264 [0.03 – 0.49]**	157 (0.054) 0.355 [0.04 – 0.67]	**881 (<0.001)** **0.592 [0.43 – 0.71]**
Extracellular diffusivity	Caudate	1.39 (0.09)	1.58 (0.24)	1.42 (0.09)	298 (0.277) -0.131 [-0.36 – -0.01]	**169 (0.015)** **0.447 [0.11 – 0.72]**	**697 (0.006)** **0.317 [0.06 – 0.55]**
	Putamen	1.47 (0.12)	1.63 (0.17)	1.42 (0.09)	490 (0.072) 0.216 [0.02 – 0.44]	**169 (0.015)** **0.447 [0.13 – 0.71]**	**842 (<0.001)** **0.534 [0.36 – 0.67]**
	Pallidum	1.67 (0.19)	1.80 (0.18)	1.53 (0.11)	**569 (0.003)** **0.358 [0.09 – 0.56]**	156 (0.060) 0.348 [0.04 – 0.65]	**893 (<0.001)** **0.610 [0.47 – 0.72]**

Abbreviations: CI, Confidence Intervals.
Pairwise comparisons were conducted with Mann–Whitney U tests; effect sizes are rank–biserial correlations (signed) with 95% CIs.
Bold indicates $p < 0.05$.

Supplementary Table 4. Descriptive statistics and non-parametric pairwise comparisons for SANDI indices (significant for total HD sample vs HC) between HD-ISS 0-1, HD-ISS 2-3, and Healthy Controls.

Data availability

This research utilised baseline data from the HD-DRUM project that has been endorsed by the Enroll-HD Scientific Oversight Committee (SOC) (14/11/2022). At the end of the HD-DRUM project, the coded study data will be shared and made accessible to the research community via the Enroll-HD specific data request process. WAND data are publicly available (*https://git.cardiff.ac.uk/cubric/wand*).

Acknowledgements

We would like to thank Amy Dangerfield, Allison Cooper and Sonya Foley-Bozorgzad for their help with data collection as well as Derek Jones and John Evans for their advice and support with regards to the implementation of MRI data acquisition protocols. We would like to thank the following clinical and administrative staff at the participating patient identification centres for their help with identifying suitable patients for the study: Eileen Donovan, Kim Munnery, and Jane Davies from the Cardiff HD clinic; Jessica Prado Mota from the Royal Devon University Healthcare NHS Foundation Trust in Exeter; Jenni Burns from the Walton Centre NHS Foundation Trust in Liverpool; Natalie Rosewell, Anya Soonderpershad, and Dr Liz Coulthard from the Bristol Brain Centre; Claire Tilley and Dr Hugh Rickards from the Birmingham and Solihull Mental Health NHS Foundation Trust. In addition, we would like to thank all Public Involvement contributors and the members of the Enroll-HD Scientific Oversight Committee for their input into the study as well as all participants for their generous time commitment to help us conducting this research.

Additional information

Funding

This work was supported by a National Institute for Health Research (NIHR) and Health and Care Research Wales (HCRW) Advanced Fellowship to CM-B (grant number: NIHR-FS(A)- 2022). The Centre for Trials Research at Cardiff University receives infrastructure funding from HCRW. MP is supported by the UKRI Future Leaders Fellowship MR/T020296/2. CC was funded by a Wellcome Trust PhD studentship (204005/Z/16/Z) and LL by a PhD studentship of the School of Psychology at Cardiff University. The WAND project was funded by a Wellcome Trust Investigator Award (096646/Z/11/Z), a Wellcome Trust Strategic Award (104943/Z/14/Z), and a Wellcome Discovery Awards (227882/Z/23/Z and 317797/Z/24/Z).

Funding

Funder	Grant reference number	Author
Health and Care Research Wales (HCRW)	NIHR-FS(A)-2022	Claudia Metzler-Baddeley
UKRI	MR/T020296/2	Marco Palombo
Wellcome Trust (WT)	https://doi.org/10.35802/204005	Chiara Casella
Wellcome Trust (WT)	https://doi.org/10.35802/104943	Carolyn McNabb

Author ORCID iDs

Claudia Metzler-Baddeley: https://orcid.org/0000-0002-8646-1144

References

1. **Rüb U,** Seidel K, Heinsen H, Vonsattel JP, den Dunnen WF, Korf HW (2016) Huntington's disease (HD): the neuropathology of a multisystem neurodegenerative disorder of the human brain. *Brain Pathology* **26**:726-740 https://doi.org/10.1111/bpa.12426 | PubMed

2. **Tabrizi SJ,** Scahill RI, Durr A, et al. (2011) Biological and clinical changes in premanifest and early stage Huntington's disease in the TRACK-HD study: the 12-month longitudinal analysis. *Lancet Neurol* **10**:31-42 https://doi.org/10.1016/S1474-4422(10)70276-3 | PubMed
3. **Roos RAC** (2010) Huntington's disease: A clinical review. *Orphanet J Rare Dis* **5** https://doi.org/10.1186/1750-1172-5-40 | PubMed
4. **Walker FO** (2007) Huntington's disease. *The Lancet* **369**:218-228 https://doi.org/10.1016/S0140-6736(07)60111-1 | PubMed
5. **Ross CA,** Aylward EH, Wild EJ, et al. (2014) Huntington disease: Natural history, biomarkers and prospects for therapeutics. *Nat Rev Neurol* **10**:204-216 https://doi.org/10.1038/nrneurol.2014.24 | PubMed
6. **Aylward EH,** Liu D, Nopoulos PC, et al. (2012) Striatal volume contributes to the prediction of onset of Huntington disease in incident cases. *Biol Psychiatry* **71**:822-828 https://doi.org/10.1016/j.biopsych.2011.07.030 | PubMed
7. **Tan B,** Shishegar R, Poudel GR, Fornito A, Georgiou-Karistianis N (2021) Cortical morphometry and neural dysfunction in Huntington's disease: a review. *Eur J Neurol* **28**:1406-1419 https://doi.org/10.1111/ene.14648 | PubMed
8. **Kinnunen KM,** Schwarz AJ, Turner EC, et al. (2021) Volumetric MRI-Based Biomarkers in Huntington's Disease: An Evidentiary Review. *Front Neurol* **12** https://doi.org/10.3389/fneur.2021.712555 | PubMed
9. **Wilkes FA,** Abaryan Z, Ching CRK, et al. (2019) Striatal morphology and neurocognitive dysfunction in Huntington disease: The IMAGE-HD study. *Psychiatry Res Neuroimaging* **291**:1-8 https://doi.org/10.1016/j.pscychresns.2019.07.003 | PubMed
10. **Scahill RI,** Zeun BMBS P, Osborne-Crowley K, et al. (2020) Biological and clinical characteristics of gene carriers far from predicted onset in the Huntington's disease Young Adult Study (HD-YAS): a cross-sectional analysis. *Lancet Neurol* **19** https://doi.org/10.1016/S1474-4422(20)30143-5 | PubMed
11. **Paulsen JS,** Langbehn DR, Stout JC, et al. (2008) Detection of Huntington's disease decades before diagnosis: The Predict-HD study. *J Neurol Neurosurg Psychiatry* **79**:874-880 https://doi.org/10.1136/jnnp.2007.128728 | PubMed
12. **Biglan KM,** Zhang Y, Long JD, et al. (2013) Refining the diagnosis of huntington disease: The PREDICT-HD study. *Front Aging Neurosci* **5**:1-8 https://doi.org/10.3389/fnagi.2013.00012 | PubMed
13. **Tabrizi SJ,** Langbehn DR, Leavitt BR, et al. (2009) Biological and clinical manifestations of Huntington's disease in the longitudinal TRACK-HD study: cross-sectional analysis of baseline data. *Lancet Neurol* **8**:791-801 https://doi.org/10.1016/S1474-4422(09)70170-X | PubMed
14. **Tabrizi SJ,** Reilmann R, Roos RA, et al. (2012) Potential endpoints for clinical trials in premanifest and early Huntington's disease in the TRACK-HD study: analysis of 24 month observational data. *Lancet Neurol* **11**:42-53 https://doi.org/10.1016/S1474-4422(11)70263-0 | PubMed
15. **Tabrizi SJ,** Scahill RI, Owen G, et al. (2013) Predictors of phenotypic progression and disease onset in premanifest and early-stage Huntington's disease in the TRACK-HD study: Analysis of 36-month observational data. *Lancet Neurol* **12**:637-649 https://doi.org/10.1016/S1474-4422(13)70088-7 | PubMed
16. **Tabrizi SJ,** Estevez-Fraga C, van Roon-Mom WMC, et al. (2022) Potential disease-modifying therapies for Huntington's disease: lessons learned and future opportunities. *Lancet Neurol* **21**:645-658 https://doi.org/10.1016/S1474-4422(22)00121-1 | PubMed
17. **Vonsattel PJG,** Keller C, Cortes Ramirez PE (2011) Huntington's disease-neuropathology. In: Weiner WJ, Tolosa E (Eds). *Handbook of Clinical Neurology* **100** pp. 83-100
18. **Liu CF,** Younes L, Tong XJ, et al. (2023) Longitudinal imaging highlights preferential basal ganglia circuit atrophy in Huntington's disease. *Brain Commun* **5** https://doi.org/10.1093/braincomms/fcad214 | PubMed

19. **Johnson EB,** Ziegler G, Penny W, et al. (2021) Dynamics of Cortical Degeneration Over a Decade in Huntington's Disease. *Biol Psychiatry* **89**:807-816 https://doi.org/10.1016/j.biopsych.2020.11.009 | PubMed

20. **Estevez-Fraga C,** Scahill R, Rees G, Tabrizi SJ, Gregory S (2021) Diffusion imaging in Huntington's disease: Comprehensive review. *J Neurol Neurosurg Psychiatry* **92**:62-69 https://doi.org/10.1136/jnnp-2020-324377

21. **Tabrizi SJ,** Schobel S, Gantman EC, et al. (2022) A biological classification of Huntington's disease: the Integrated Staging System. *Lancet Neurol* **21**:632-644 https://doi.org/10.1016/S1474-4422(22)00120-X | PubMed

22. **Myers RH,** Vonsattel JP, Paskevich PA, et al. (1991) Decreased Neuronal and Increased Oligodendroglial Densities in Huntington's Disease Caudate Nucleus. *J Neuropathol Exp Neurol* **50**:729-742 https://doi.org/10.1097/00005072-199111000-00005 | PubMed

23. **Vis JC,** Schipper E, de Boer-van H, et al. (2005) Expression pattern of apoptosis-related markers in Huntington's disease. *Acta Neuropathol* **109**:321-328 https://doi.org/10.1007/s00401-004-0957-5 | PubMed

24. **Vis JC,** Nicholson LFB, Faull RLM, Evans WH, Severs NJ, Green CR (1998) Connexin expression in Huntington's diseased human brain. *Cell Biol Int* **22**:837-847 https://doi.org/10.1006/cbir.1998.0388 | PubMed

25. **Simmons DA,** Casale M, Alcon B, Pham N, Narayan N, Lynch G (2007) Ferritin accumulation in dystrophic microglia is an early event in the development of Huntington's Disease. *Glia* **55**:1074-1084 https://doi.org/10.1002/glia.20526 | PubMed

26. **Sapp E,** Kegel KB, Aronin N, et al. (2001) Early and Progressive Accumulation of Reactive Microglia in the Huntington Disease Brain. *J Neuropathol Exp Neurol* **60**:161-172 https://doi.org/10.1093/jnen/60.2.161 | PubMed

27. **Le Bihan D,** Turner R, Moonen CTW, Pekar J (1991) Imaging of diffusion and microcirculation with gradient sensitization: Design, strategy, and significance. *Journal of Magnetic Resonance Imaging* **1**:7-28 https://doi.org/10.1002/jmri.1880010103 | PubMed

28. **Basser PJ,** Mattiello J, LeBihan D (1994) MR diffusion tensor spectroscopy and imaging. *Biophys J* **66**:259-267 https://doi.org/10.1016/S0006-3495(94)80775-1 | PubMed

29. **Basser PJ,** Pierpaoli C (1996) Microstructural and Physiological Features of Tissues Elucidated by Quantitative-Diffusion-Tensor MRI. *J Magn Reson B* **111**:209-219 https://doi.org/10.1006/jmrb.1996.0086 | PubMed

30. **Georgiou-Karistianis N,** Gray MA, Domínguez D JF, et al. (2013) Automated differentiation of pre-diagnosis Huntington's disease from healthy control individuals based on quadratic discriminant analysis of the basal ganglia: The IMAGE-HD study. *Neurobiol Dis* **51**:82-92 https://doi.org/10.1016/j.nbd.2012.10.001 | PubMed

31. **Hobbs NZ,** Cole JH, Farmer RE, et al. (2013) Evaluation of multi-modal, multi-site neuroimaging measures in Huntington's disease: Baseline results from the PADDINGTON study. *Neuroimage Clin* **2**:204-211 https://doi.org/10.1016/j.nicl.2012.12.001 | PubMed

32. **Jones DK,** Alexander DC, Bowtell R, et al. (2018) Microstructural imaging of the human brain with a 'super-scanner': 10 key advantages of ultra-strong gradients for diffusion MRI. *Neuroimage* **182**:8-38 https://doi.org/10.1016/j.neuroimage.2018.05.047 | PubMed

33. **Assaf Y,** Basser PJ (2005) Composite hindered and restricted model of diffusion (CHARMED) MR imaging of the human brain. *Neuroimage* **27**:48-58 https://doi.org/10.1016/j.neuroimage.2005.03.042 | PubMed

34. **Zhang H,** Schneider T, Wheeler-Kingshott CA, Alexander DC (2012) NODDI: Practical in vivo neurite orientation dispersion and density imaging of the human brain. *Neuroimage* **61**:1000-1016 https://doi.org/10.1016/j.neuroimage.2012.03.072 | PubMed

35. **Martinez-Heras E,** Grussu F, Prados F, Solana E, Llufriu S (2021) Diffusion-Weighted Imaging: Recent Advances and Applications. *Seminars in Ultrasound, CT and MRI* **42**:490-506 https://doi.org/10.1053/j.sult.2021.07.006 | PubMed

36. **Daducci A,** Dal Palu A, Lemkaddem A, Thiran JP (2015) COMMIT: Convex Optimization Modeling for Microstructure Informed Tractography. *IEEE Trans Med Imaging* **34**:246-257 https://doi.org/10.1109/TMI.2014.2352414 | PubMed

37. **Zhang J,** Gregory S, Scahill RI, et al. (2018) In vivo characterization of white matter pathology in premanifest huntington's disease. *Ann Neurol* **84**:497-504 https://doi.org/10.1002/ana.25309 | PubMed

38. **Palombo M,** Ianus A, Guerreri M, et al. (2020) SANDI: A compartment-based model for non-invasive apparent soma and neurite imaging by diffusion MRI. *Neuroimage* **215**:116835 https://doi.org/10.1016/j.neuroimage.2020.116835 | PubMed

39. **Koller K,** Rudrapatna U, Chamberland M, et al. (2021) MICRA: Microstructural image compilation with repeated acquisitions. *Neuroimage* **225**:117406 https://doi.org/10.1016/j.neuroimage.2020.117406 | PubMed

40. **Ianuş A,** Carvalho J, Fernandes FF, et al. (2022) Soma and Neurite Density MRI (SANDI) of the in-vivo mouse brain and comparison with the Allen Brain Atlas. *Neuroimage* **254** https://doi.org/10.1016/j.neuroimage.2022.119135 | PubMed

41. **Krijnen EA,** Russo AW, Salim Karam E, et al. (2023) Detection of grey matter microstructural substrates of neurodegeneration in multiple sclerosis. *Brain Commun* **5** https://doi.org/10.1093/braincomms/fcad153 | PubMed

42. **Margoni M,** Pagani E, Preziosa P, et al. (2023) In vivo quantification of brain soma and neurite density abnormalities in multiple sclerosis. *J Neurol* **270**:433-445 https://doi.org/10.1007/s00415-022-11386-3 | PubMed

43. **Zeng JY,** Huang HW, Zhuang SP, et al. (2025) Soma and neurite density imaging detects brain microstructural impairments in amyotrophic lateral sclerosis. *Eur J Radiol* **184** https://doi.org/10.1016/j.ejrad.2025.111981 | PubMed

44. **Barakovic M,** Weigel M, Cagol A, et al. (2024) A novel imaging marker of cortical "cellularity" in multiple sclerosis patients. *Sci Rep* **14**:9848 https://doi.org/10.1038/s41598-024-60497-6 | PubMed

45. **Byrne LM,** Rodrigues FB, Johnson EB, et al. (2018) Evaluation of mutant huntingtin and neurofilament proteins as potential markers in Huntington's disease. *Sci Transl Med* **10** https://doi.org/10.1126/scitranslmed.aat7108 | PubMed

46. **Sampedro F,** Pérez-Pérez J, Martínez-Horta S, et al. (2021) Cortical microstructural correlates of plasma neurofilament light chain in Huntington's disease. *Parkinsonism Relat Disord* **85**:91-94 https://doi.org/10.1016/j.parkreldis.2021.03.008 | PubMed

47. **Bechtel N,** Scahill RI, Rosas HD, et al. (2010) Tapping linked to function and structure in premanifest and symptomatic Huntington disease. *Neurology* **75**:2150-2160 https://doi.org/10.1212/WNL.0b013e3182020123 | PubMed

48. **Warner JH,** Long JD, Mills JA, et al. (2022) Standardizing the CAP Score in Huntington's Disease by Predicting Age-at-Onset. *J Huntingtons Dis* **11**:153-171 https://doi.org/10.3233/JHD-210475 | PubMed

49. **Ioakeimidis V,** Busse M, Drew CJG, et al. (2024) Protocol for a randomised controlled unblinded feasibility trial of HD-DRUM: a rhythmic movement training application for cognitive and motor symptoms in people with Huntington's disease. *BMJ Open* **14**:e082161 https://doi.org/10.1136/bmjopen-2023-082161 | PubMed

50. **Casella C,** Chamberland M, Laguna PL, et al. (2022) Mutation-related magnetization-transfer, not axon density, drives white matter differences in premanifest Huntington disease: Evidence from in vivo ultra-strong gradient MRI. *Hum Brain Mapp* 3439-3460 https://doi.org/10.1002/hbm.25859 | PubMed

51. **McNabb CB,** Driver ID, Hyde V, et al. (2025) WAND: A multi-modal dataset integrating advanced MRI, MEG, and TMS for multi-scale brain analysis. *Sci Data* **12**:220 https://doi.org/10.1038/s41597-024-04154-7 | PubMed

52. **Siesling S,** Van Vugt JPP, Zwinderman KAH, Kieburtz K, Roos RAC (1998) Unified Huntington's disease rating scale: A follow up. *Movement Disorders* **13**:915-919 https://doi.org/10.1002/mds.870130609 | PubMed

53. **Nasreddine ZS,** Phillips NA, Bédirian V, et al. (2005) The Montreal Cognitive Assessment, MoCA: A Brief Screening Tool For Mild Cognitive Impairment. *J Am Geriatr Soc* **53**:695-699 https://doi.org/10.1111/j.1532-5415.2005.53221.x | PubMed

54. **Wechsler D** (2011) Test of Premorbid Functioning UK version (TOPF UK).

55. **Schubert R,** Fiedler H, Barallon P, Habbel B, Reilmann R (2022) F55 Q-motor speeded tapping and pointing assessments: feasibility of a dual task design. *Journal of Neurology, Neurosurgery & Psychiatry* A56.1-A56 https://doi.org/10.1136/jnnp-2022-ehdn.146

56. **Schubert R,** Rosser A, Bachoud-Lévi AC, Craufurd D, Reilmann R (2018) F63 Preliminary results from Q-MOTOR/Q-COG analyses in the repair-hd study. *ournal of Neurology, Neurosurgery & Psychiatry* A62.1-A62 https://doi.org/10.1136/jnnp-2018-EHDN.164

57. **Reilmann R,** Schubert R (2017) Motor Outcome Measures in Huntington Disease Clinical Trials. In: Feigin AS, Anderson KE (Eds). *Handbook of clinical neurology* **144** Elsevier. https://doi.org/10.1016/B978-0-12-801893-4.00018-3 | PubMed

58. **Reilmann R,** Rosser A, Kostyk S, et al. (2021) F41 The proof-hd phase 3 study: pridopidine's outcome on function in huntington disease (PROOF). *Journal of Neurology, Neurosurgery & Psychiatry* A36.1-A36 https://doi.org/10.1136/jnnp-2021-EHDN.84

59. **Reilmann R,** Anderson KE, Feigin A, et al. (2024) Safety and efficacy of laquinimod for Huntington's disease (LEGATO-HD): a multicentre, randomised, double-blind, placebo-controlled, phase 2 study. *Lancet Neurol* **23**:243-255 https://doi.org/10.1016/S1474-4422(23)00454-4 | PubMed

60. **Hermle D,** Schubert R, Barallon P, et al. (2024) Multifeature quantitative motor assessment of upper limb ataxia including drawing and reaching. *Ann Clin Transl Neurol* **11**:1097-1109 https://doi.org/10.1002/acn3.52024 | PubMed

61. **Tuch DS,** Reese TG, Wiegell MR, Makris N, Belliveau JW, Wedeen VJ (2002) High angular resolution diffusion imaging reveals intravoxel white matter fiber heterogeneity. *Magn Reson Med* **48**:577-582 https://doi.org/10.1002/mrm.10268 | PubMed

62. **Smith SM** (2002) Fast robust automated brain extraction. *Hum Brain Mapp* **17**:143-155 https://doi.org/10.1002/hbm.10062 | PubMed

63. **Tournier JD,** Smith R, Raffelt D, et al. (2019) MRtrix3: A fast, flexible and open software framework for medical image processing and visualisation. *Neuroimage* **202**:116137 https://doi.org/10.1016/j.neuroimage.2019.116137 | PubMed

64. **Leemans A,** Jeurissen B, Sijbers J, Jones DK (2009) ExploreDTI: a graphical toolbox for processing, analyzing, and visualizing diffusion MR data. In: ISMRM.

65. **Sairanen V,** Leemans A, Tax CMW (2018) Fast and accurate Slicewise OutLIer Detection (SOLID) with informed model estimation for diffusion MRI data. *Neuroimage* **181**:331-346 https://doi.org/10.1016/j.neuroimage.2018.07.003 | PubMed

66. **Andersson JLR,** Skare S, Ashburner J (2003) How to correct susceptibility distortions in spin-echo echo-planar images: application to diffusion tensor imaging. *Neuroimage* **20**:870-888 https://doi.org/10.1016/S1053-8119(03)00336-7 | PubMed

67. **Smith SM,** Jenkinson M, Woolrich MW, et al. (2004) Advances in functional and structural MR image analysis and implementation as FSL. *Neuroimage* **23**:S208-S219 https://doi.org/10.1016/j.neuroimage.2004.07.051 | PubMed

68. **Andersson JLR,** Sotiropoulos SN (2016) An integrated approach to correction for off-resonance effects and subject movement in diffusion MR imaging. *Neuroimage* **125**:1063-1078 https://doi.org/10.1016/j.neuroimage.2015.10.019 | PubMed

69. **Kellner E,** Dhital B, Kiselev VG, Reisert M (2016) Gibbs-ringing artifact removal based on local subvoxel-shifts. *Magn Reson Med* **76**:1574-1581 https://doi.org/10.1002/mrm.26054 | PubMed

70. **Cordero-Grande L,** Christiaens D, Hutter J, Price AN, Hajnal J V (2019) Complex diffusion-weighted image estimation via matrix recovery under general noise models. *Neuroimage* **200**:391-404 https://doi.org/10.1016/j.neuroimage.2019.06.039 | PubMed

71. **Veraart J,** Fieremans E, Novikov DS (2016) Diffusion MRI noise mapping using random matrix theory. *Magn Reson Med* **76**:1582-1593 https://doi.org/10.1002/mrm.26059 | PubMed

72. **Veraart J,** Novikov DS, Christiaens D, Ades-aron B, Sijbers J, Fieremans E (2016) Denoising of diffusion MRI using random matrix theory. *Neuroimage* **142**:394-406 https://doi.org/10.1016/j.neuroimage.2016.08.016 | PubMed

73. **Fischl B.** (2012) FreeSurfer. *Neuroimage* **62**:774-781 https://doi.org/10.1016/j.neuroimage.2012.01.021 | PubMed

74. **Jenkinson M** (2002) Improved Optimization for the Robust and Accurate Linear Registration and Motion Correction of Brain Images. *Neuroimage* **17**:825-841 https://doi.org/10.1016/S1053-8119(02)91132-8

75. **JASP Team** (2023) Jasp.

76. **R Core Team** (2024) R: A Language and Environment for Statistical Computing. R Foundation for Statistical Computing. https://doi.org/10.32614/r.manuals

77. **RStudio Team** (2024) RStudio: Integrated Development for R. RStudio, PBC.

78. **IBM Corp** (2024) IBM SPSS Statistics for Windows. IBM Corp.

79. **Benjamini Y,** Hochberg Y (1995) Controlling the False Discovery Rate: A Practical and Powerful Approach to Multiple Testing. *J R Stat Soc Series B Stat Methodol* **57**:289-300 https://doi.org/10.1111/j.2517-6161.1995.tb02031.x

80. **Lakens D** (2014) Performing high-powered studies efficiently with sequential analyses. *Eur J Soc Psychol* **44**:701-710 https://doi.org/10.1002/ejsp.2023

81. **Preacher KJ,** MacCallum RC (2002) Exploratory Factor Analysis in Behavior Genetics Research: Factor Recovery with Small Sample Sizes. *Behav Genet* **32**:153-161 https://doi.org/10.1023/A:1015210025234 | PubMed

82. **de Winter JCF,** Dodou D, Wieringa PA (2009) Exploratory Factor Analysis With Small Sample Sizes. *Multivariate Behav Res* **44**:147-181 https://doi.org/10.1080/00273170902794206 | PubMed

83. **Matz OC,** Spocter M (2022) The Effect of Huntington's Disease on the Basal Nuclei: A Review. *Cureus* **14** https://doi.org/10.7759/cureus.24473 | PubMed

84. **Sánchez-Castañeda C,** Cherubini A, Elifani F, et al. (2013) Seeking huntington disease biomarkers by multimodal, cross-sectional basal ganglia imaging. *Hum Brain Mapp* **34**:1625-1635 https://doi.org/10.1002/hbm.22019 | PubMed

85. **Fricker M,** Tolkovsky AM, Borutaite V, Coleman M, Brown GC (2018) Neuronal Cell Death. *Physiol Rev* **98**:813-880 https://doi.org/10.1152/physrev.00011.2017 | PubMed

86. **Kerr JFR,** Wyllie AH, Currie AR (1972) Apoptosis: A Basic Biological Phenomenon with Wideranging Implications in Tissue Kinetics. *Br J Cancer* **26**:239-257 https://doi.org/10.1038/bjc.1972.33 | PubMed

87. **Klaus A,** Alves da Silva J, Costa RM. (2019) What, If, and When to Move: Basal Ganglia Circuits and Self-Paced Action Initiation. *Annu Rev Neurosci* **42**:459-483 https://doi.org/10.1146/annurev-neuro-072116-031033 | PubMed

88. **Olesen JL,** Østergaard L, Shemesh N, Jespersen SN (2022) Diffusion time dependence, power-law scaling, and exchange in gray matter. *Neuroimage* **251**:118976 https://doi.org/10.1016/j.neuroimage.2022.118976 | PubMed

89. **Jelescu IO,** de Skowronski A, Geffroy F, Palombo M, Novikov DS (2022) Neurite Exchange Imaging ((NEXI): A minimal model of diffusion in gray matter with inter-compartment water exchange. *Neuroimage* **256** https://doi.org/10.1016/j.neuroimage.2022.119277 | PubMed

90. **Schiavi S,** Palombo M, Zacà D, et al. (2023) Mapping tissue microstructure across the human brain on a clinical scanner with soma and neurite density image metrics. *Hum Brain Mapp* **44**:4792-4811 https://doi.org/10.1002/hbm.26416 | PubMed

Peer reviews

Reviewer #1 (Public review):

(1) In this study, the authors aimed at characterizing Huntington's Disease (HD) - related microstructural abnormalities in the basal ganglia and thalami as revealed using Soma and Neurite Density Imaging (SANDI) indices (apparent soma density, apparent soma size, extracellular water signal fraction, extracellular diffusivity, apparent neurite density, fractional anisotropy and mean diffusivity).

(2) The study implements a novel biophysical diffusion model that extends up-to-date methodologies and presents a significant potential for quantifying neurodegenerative processes of the grey matter of the human brain in vivo. The authors comment on the usefulness of this technique in other pathologies, but they exemplify only with multiple sclerosis. Further development of this, building evidence should be provided.

(3) Study found that HD-related neurodegeneration in the striatum accounted significantly for striatal atrophy and correlated with motor impairments. HD was associated with reduced soma density, increased apparent soma size and extracellular signal fraction in the basal ganglia, but not in the thalami. Additionally, these affects were larger at manifest stage.

(4) The results of this work demonstrate the impact of HD on basal ganglia and thalami which can be further explored as a non-invasive biomarker of disease progression. Additionally, the study shows that SANDI can be used to explore grey matter microstructure in a variety of neurological conditions.

Comments on revised version.

I have no further comments. Thank you

https://doi.org/10.7554/eLife.107661.2.sa2

Reviewer #3 (Public review):

Summary:

Ioakeimidis and colleagues studied miscrostructural abnormalities in N=56 Huntington's disease (HD) patients compared to N=57 normative controls. The authors used a powerful MRI Connectom scanner and applied the SANDI model to estimate the soma size, neurite size, soma density, and extracellular fraction in key subcortical nuclei related to HD. In the striatum, they found decreased soma density and increased soma size, which also seemed to become more pronounced in advanced HD individuals in the final exploratory analyses. The authors conducted important analyses to find whether the SANDI measures correlate with clinical scores (i.e., QMotor) and whether the variance of the striatal volume is explained by the SANDI measures. They found a relationship of SANDI measures to both.

Strengths:

The study is both innovative and of high interest for the HD community. The authors provide a rich pool of statistical analyses and results which anticipate the questions that may emerge in the HD research community. Statistics are carefully chosen and image processing is done with state-of-the-art methods and tools. The sample size gives sufficient credibility to the findings. Altogether, I think this study sets a milestone in the attempts of the HD community to understand neuropathological processes with non-invasive methods, and extends the current knowledge of microstructural anomalies identified in HD with diffusion MRI. More importantly, the newly identified anomalies in soma size and soma density open new avenues for studying these biological effects further, and perhaps develop these biomarkers for use in clinical trials.

Weaknesses:

(1) An important question is whether the SANDI measures, which require an expensive scanner and elaborate processing, are better biomarkers than the more traditional DTI measures. Can the authors compare the effect size of FA/MD with SANDI measures. In some of the plots and tables, FA/MD seem to have comparable, if not higher, correlations with QMotor or CAP scores. On the same vein, it is unclear whether DTI measures were included in hierarchical stepwise regression. I wonder if the stepwise models may have picked up FA/MD instead of SANDI measures if they are given a chance. Overall, I hope the authors can discuss their findings also in this light of cost vs. benefit of adopting SANDI in future studies, which is an important topic for clinical trials.

(2) Similar to the above point, it is very important to consider how strong the biomarking signal is from SANDI measures compared to the good old striatal volume. Some plots seem to indicate that volumes still have the highest correlation with QMotor, and highest effect size in group comparisons. It would be helpful for the community to know where do the new SANDI measures stand compared to the most typically used volumes in terms of effect size.

(3) The diffusion measures are inevitably correlated to some degree. Please provide a correlation matrix in supplementary material including all DWI measures to enable readers to understand better how similar SANDI measures are between each other or vs. other DTI measures. Perhaps adding volumes to this correlation matrix may also be a good future reference.

(4) ISS stages:

(a) The online ISS calculator requires cut-offs derived from the longitudinal Freesurfer pipeline, while the authors do not have longitudinal data. Thus, the ISS classification might be inaccurate to some degree if the authors used the FS cross-sectional pipeline. Please review this issue and see if updated cut-offs should be used to classify participants.

(b) Were there really no participants with ISS 0 among 56 HD individuals, please clarify in the manuscript?

(c) A note on terminology that might be confusing to some readers. According to the creators of ISS, the ISS stages are created for research only, they are not used or applied in the clinic. On the other hand, the terms "premanifest" and "manifest" have a clinical meaning, typically based on the diagnostic confidence level. The assignment of ISS0-1 to premanifest and ISS2-3 to manifest may create some non-trivial confusion, if not opposition, in some segments the HD community. The authors can keep their current terminology but will need to at least clarify to the reader that this assignment is speculative, does not fully match the clinically-based categories, and should not be confused with similarly named groups in the previous literature.

Comments on revised version.

The authors have moved to address many points from reviewers. The manuscript had indeed become more objective, transparent, and to the point. The amount of information and analyses is large, which perhaps is inevitable when new methods are being tested for the first time in a neurodegenerative disease.

https://doi.org/10.7554/eLife.107661.2.sa1

Author response:

The following is the authors' response to the original reviews.

> ***Reviewer #1:***
>
> *(1) The biological and/or mathematical meaning of the Soma and Neurite Density Imaging (SANDI) indices (apparent soma density, apparent soma size, extracellular water signal fraction, extracellular diffusivity, apparent neurite density, fractional anisotropy, and mean diffusivity) should be briefly introduced for those less familiar with this novel technique.*

Further explanations about the biological and mathematical meaning of the SANDI indices were added to the introduction on page 6.

> *(2) The study implements a novel biophysical diffusion model that extends up-to-date methodologies and presents a significant potential for quantifying neurodegenerative processes of the grey matter of the human brain in vivo. The authors comment on the usefulness of this technique in other pathologies, but they exemplify it only with multiple sclerosis. Further development of this, building evidence, should be provided.*

Clinical applications of SANDI have primarily focused on MS. However, since preparation of the manuscript, one study has been published reporting reductions in apparent soma density and white and grey matter specific differences in apparent soma size in amyotrophic lateral sclerosis (ALS) (Zeng et al., Eur J Radiol 2025, 10.1016/j.ejrad.2025.111981). These findings accord with the loss of motor neurons and glial responses in ALS. We have added this study to the introduction of SANDI on page 7.

> *(3) Why are the basal ganglia compared against thalami? The rationale of this decision is missing.*

The thalami were selected as control regions based on the established trajectory of neurodegeneration in HD, which begins with early loss of medium spiny neurons in the striatum and later extends to surrounding structures, including the putamen and thalamus. Given that most participants in our study were at early disease stages, we assumed the thalami would remain relatively unaffected in this sample. This explanation has been added to the introduction on page 7.

> *(4) The use of bullet points is unusual for a scientific paper format.*

Bullet points have been removed throughout the manuscript.

> *(5) The authors mention that they eroded the boundaries of the subcortical masks. Providing the details and parameters of this erosion would be beneficial.*

Details of the default parameters of the FSL erode function that was used have been added to the method section on page 13.

> *(6) In the conclusion, the authors state that their results will bridge the gap between histopathological findings and in vivo imaging, but it would be helpful if they could*

> *briefly explain how they imagine such a bridge (e.g., which kind of comparisons or correlations) and whether there exists any literature in this regard so far.*

We have added the following brief explanation to the conclusion on page 26: "Although conventional MRI lacks the resolution to directly capture histopathology, advanced biophysical models such as SANDI may help bridge this gap by providing biologically interpretable parameters that reflect tissue composition and capture histopathological changes *in vivo*."

> *(7) The scale is missing in Figure 3.*

The scale has been added to Figure 3.

> *(8) In general, the work would benefit from a better organization and potentially a smaller number of figures and tables.*

The manuscript has been re-edited to improve the readability and organization throughout and the number of figures and tables were reduced by moving some of them to the Supplementary Material (old Tables 2 and 5 are now Supplementary Tables 2 and 3, old Figure 3 is now Supplementary Figure 1).

> ***Reviewer #2:***
>
> *Certain aspects of the study would benefit from clarification:*
>
> *(1) Scanner and acquisition consistency: While HD data are from the WAND study, it is not clear whether controls were scanned on the same scanner or protocol. Given the use of model-derived metrics (especially SANDI), differences in scanner or acquisition could introduce confounds. From the text, the HD participants are explicitly said to come from the WAND study (a longitudinal HD cohort). On the other hand, while the HC participants are described as age-matched controls, the paper does not clearly state whether they were scanned in the same study (i.e., WAND), on the same scanner, or with the same acquisition protocol. This ambiguity is potentially problematic, especially since they use model-derived diffusion metrics that can be very sensitive to scanner hardware, gradient strengths, and protocol settings. If the WAND HD data were acquired on a specific scanner (e.g., 3T Connectom) and the HCs were not, then differences in SANDI/DTI metrics might reflect scanner bias, not disease pathology. This is particularly critical in SANDI, which is sensitive to high b-values and SNR. It would strengthen the manuscript to explicitly state whether the HD and control data were acquired using the same scanner model, sequence, and protocol, and ideally at the same site. If this were not the case, the authors should include this as a limitation and discuss any harmonization strategies applied (e.g., ComBat, covariate modeling, etc).*

For harmonization and comparison purposes, HD and control data were acquired using the same strong gradient (300mT/m) 3T Connectom MRI system at CUBRIC with the same acquisition protocols and sequences. It should also be noted that the Connectom scanner has not had any software upgrades that could introduce scanner biases in data acquired at different time points. This is now made explicit on page 8 by stating that all MRI data for all participants were acquired on the same MRI system using the same acquisition protocols, and on page 10 by stating that all HD and HC MRI data included in our analyses were acquired on the same 3T Siemens Connectom scanner at CUBRIC using the same acquisition protocols described in this section.

> *Also, although it offers novel and biologically informative markers, widespread clinical translation still faces hurdles. For instance, the study used a 3T Connectom scanner (300mT/m gradients), which is not widely available. Reproduction of these results in standard 3T clinical scanners would be a great addition, in scenarios with lower*

> *resolution, less precise parameter recovery, and longer scans if SNR needs to be maintained.*

We agree that for clinical adoption it is important to demonstrate that HD-related SANDI differences can also be detected on clinical MRI systems and do not require ultra-strong gradient imaging. While we have not collected such data in people with HD, we have demonstrated the feasibility of modelling SANDI metrics from multi-shell diffusion-weighted imaging acquired on a clinical 3T MRI (maximum b-value of 6,000 s/mm^2) in healthy adults and people with MS (Schiavi et al 2023, *https://doi.org/10.1002/hbm.26416*). Furthermore, Zeng et al 2025, reported significant differences in SANDI metrics acquired on a 3T MRI Prisma system between individuals with ALS and healthy controls (maximum b-value of 3,000 s/mm^2).

Two additional studies demonstrated that SANDI could be implemented and microstructural differences could be detected in MS using 3T scanners with standard gradient strength (Barakovic et al., 2024; Margoni et al., 2023). Collectively, these findings indicate that SANDI can be applied on clinical scanners, particularly as clinical systems move toward stronger gradient capabilities such as Siemens Magnetom Cima.X. These explanations can be found under the clinical implication section in the Discussion on page 25.

> *(2) Limitations of HD-ISS staging resolution and group separation:*
>
> *The use of HD-ISS staging to anchor progression analyses is conceptually appropriate, but, in practice, the sample is quite limited.*
>
> *(a) Only 26-27 out of 56 gene-positive participants could be assigned HD-ISS stages, and none were classified into stages 0 or 4. This restricts the interpretation of progression to a narrow clinical window (mostly stages 1-3) and excludes over 50% of the cohort.*
>
> *(b) Furthermore, visual inspection of the scatter plots (e.g., Figures 3 and 4) reveals substantial overlap between stages 1 and 2, particularly in CAP100 and Q-Motor measures. This suggests that the separation between early disease stages may not be robust in this dataset, potentially due to limited power or phenotypic variability.*
>
> *(c) The above may lead to claims based on progression across HD-ISS stages to be overinterpreted or underpowered*
>
> *Despite this, the paper treats the staging as a reliable stratification for group comparisons. To improve clarity and transparency, I would recommend that the authors:*
>
> *(a) Acknowledge that over 50% of the HD cohort could not be classified.*
>
> *(b) Discuss whether those excluded differed from those included in key metrics.*
>
> *(c) Explicitly comment on the substantial overlap between stages 1 and 2, and limit claims about progression unless such separation is statistically supported.*
>
> *(d) Avoid overinterpreting staging-related effects without statistical support for group separability*

Re a-d) We have added to the study limitations on pages 23 ff that only 54% (30 out of 56) HD participants could be HD-ISS classified due to missing data, and provide an overview of demographic and clinical information for HD-ISS stages and unclassified individuals in Supplementary Table 1. We acknowledge that the combined groups (HD-ISS 0-1 versus HD-ISS 23) for exploratory group analyses did not represent discrete disease stages and that there was some overlap in imaging and behavioural features between them as illustrated in Figures 3, 4, and 7. We state explicitly that these exploratory findings should be interpreted

with caution and require replication in larger, prospective cohorts before SANDI metrics can be considered as potential markers of disease progression.

> *(3) Clarify regression strategy and interpretational limits of SANDI-derived regressors: While the hierarchical regression strategy is broadly appropriate, several aspects would benefit from clarification to improve both interpretability and robustness of the findings. For example:*
>
> *(a) Why were only a subset of SANDI parameters (fis and De) considered in the HC models (Figure 6), while additional metrics (fec and rs) were tested in HD models (Figures 7-8)? Including the same variables across groups could aid comparability?*

The same SANDI indices were included in regression models for HD and HC groups, Figure 7-8 report only significant predictors. This has been clarified in the figure legend and on pages 14 of the manuscript.

> *(b) Were any checks for multicollinearity (e.g., variance inflation factors) conducted? Given known interdependencies among some SANDI parameters, I wonder whether some of the reported regression coefficients may be unstable or difficult to interpret.*

Cross-correlation matrices between all imaging metrics for HD, HC, and total samples have been included to Supplementary materials Figure 3.

> *To improve transparency and interpretability, I suggest actions such as:*
>
> *(a) SANDI metrics included in the models differ between HC and HD groups, reducing comparability. Consider using consistent full models across ROIs for comparison purposes, even if some predictors are not significant.*
>
> *(b) Report the correlation structure between SANDI metrics within each group to assess multicollinearity (The potential impact of multicollinearity (e.g., between fis and rs) is not discussed)*
>
> *(c) Explicitly acknowledge the limitations imposed by parameter degeneracy in the SANDI model and clarify how the authors ensured the biological interpretability of regression outputs in this context - Beta coefficients could reflect model instability or parameter degeneracy rather than true biological effects.*

(a) The same SANDI metrics and age were included in the first regression models for HD and HC data. The first models only differed by the inclusion of TFC as estimate of disease burden for the HD data. HD and HC participants were not included in a single regression model, as our aim was not to perform formal between-group inference on regression coefficients. Instead, models were fitted separately to explore within-group associations and to descriptively compare patterns of relationships across groups. This approach avoids imposing identical model structures across groups that may differ in variance structure, disease burden, and biological coupling between SANDI metrics. We have clarified these points on page 13/14.

(b) We agree that multicollinearity is an important consideration when interpreting regression coefficients derived from microstructural models. To address this, we examined pairwise Spearman correlations between all imaging (SANDI, DTI, volume) metrics (averaged across ROIs), shown in the revised Supplementary Figure 2. As can be seen in the healthy control data, SANDI indices of apparent soma and neurite fractions showed a strong inverse correlation (rho = -0.92) and did not correlate with soma radius (rho = 0.1). All SANDI indices correlated only weakly with FA and volume and moderately with MD. This correlation pattern suggests that apparent soma density and radius capture distinct information about grey matter microstructure that differs from neurite fraction and is not captured by FA or

volume. We note in HD participants a negative correlation between soma radius and fraction, and stronger correlations between SANDI metrics and volume measures. We would argue that these reflect disease-related reorganization of micro- and macro-structural relationships rather than uniform collinearity across groups. This information has been added to the Methods, Results and Discussion sections on pages 13, 19, and 21, 23ff.

(c) We agree that regression coefficients derived from interdependent microstructural parameters should be interpreted with caution, as they may reflect shared variance or partial parameter degeneracy rather than fully independent biological effects. For this reason, we do not interpret individual beta coefficients in isolation. Instead, our conclusions focus on the consistency and directionality of associations across regions and metrics, and on the overall feasibility and sensitivity of SANDI to detect biologically meaningful variation in HD. The observed correlation structure (Supplementary Figure 2) provides important context for these interpretations and supports a multivariate, pattern-based rather than univariate reading of the results. These points have been added to the Discussion on pages 23 ff. Please also refer to our response to point (5) below.

> *(4) Preprocessing order:*
>
> *Gibbs ringing correction was applied after TOPUP and EDDY, which deviates from the commonly recommended order in diffusion MRI preprocessing. Since Gibbs artifacts are introduced by kspace truncation and affect the spatial domain, it is typically advised to perform Gibbs correction prior to geometric corrections like TOPUP and EDDY. This avoids potential blurring or propagation of ringing artifacts during resampling. Could the authors clarify the rationale for this ordering, and whether an early application of Gibbs correction was tested?*

We agree that the application of Gibbs ringing correction prior to TOPUP and EDDY correction deviates from the commonly recommended order in diffusion MRI preprocessing. However, as some of the data included in this paper were preprocessed before this consensus was agreed in the literature, we kept the preprocessing order consistent for all datasets for harmonization and comparison purposes. We have since changed the order for subsequent preprocessing of the HDDRUM data and have found comparable FA maps for data processed with Gibbs ringing correction before and after TOPUP and EDDY correction.

> *(5) Expand on SANDI model assumptions:*
>
> *SANDI is presented as being used for the very first time in this problem. However, a vague explanation is given: "using all the default settings". Given the novelty of applying SANDI in a clinical HD context, the manuscript would benefit from a discussion of the model's key assumptions and limitations. For instance:*
>
> *(a) The potential degeneracy between fis and rs in the absence of protocol features (e.g., long Δ or high b) that can disambiguate them.*
>
> *(b) Whether a dot compartment was included, and the implications of excluding it for the interpretation of rs or fis.*
>
> *(c) The lack of exchange modeling or fixed stick diffusivity, and how these may bias compartment estimates (particularly in diseased or aging tissue).*
>
> *(d) Any steps taken to verify robustness or identifiability (e.g., simulations, synthetic fitting). These issues are not flaws in the method, but they do affect how confident we can be in interpreting fis/rs as markers of neuron loss or glial hypertrophy, especially given the subtle group differences and the potential for biological heterogeneity in HD. Even a brief acknowledgment would strengthen the manuscript and provide useful context to readers less familiar with multicompartment modeling.*

We thank the reviewer for this constructive suggestion and fully agree that, because this is the first application of SANDI in our clinical HD cohort, the manuscript should more explicitly describe the model assumptions, potential identifiability limitations under our protocol, and the implications for biological interpretation.

We have revised the Methods (pages 11-12) and Discussion (page 24) to (i) specify the exact SANDI implementation used (the SANDI MATLAB toolbox, available at: *https://github.com/palombom/SANDI-Matlab-Toolbox-Latest-Release*), (ii) describe which components are included in the default formulation and the key modelling assumptions, and (iii) add a dedicated "Limitations and interpretability" paragraph addressing points (a–d) below. We also avoid the previous shorthand "default settings" and provide a clear description of the fitting setup.

"The SANDI model [Palombo M. et al, NeuroImage 2020] assumes three compartments, namely intra-neurite signal modelled as diffusion inside impermeable randomly oriented sticks, intra-soma signal modelled as restricted diffusion inside spheres, and extra-cellular signal modelled as Gaussian isotropic diffusion. The direction-averaged (or spherical mean) normalized diffusion signal has thus the following expression:

$$S(b) = f_{is}A_{sphere}(b, r_s, D_{is}) + f_{in}A_{stick}(b, D_{in}) + f_{ec}A_{ball}(b, D_e)$$

where $f_{in} + f_{is} + f_{ec} = 1$; A_{stick} and A_{sphere} are the normalized, directionally-averaged (or spherical mean) signals for restricted diffusion within neurites and soma, respectively and A_{ball} is the normalized, directionally-averaged (or spherical mean) signal of the extra-cellular space. The specific expressions are given in [Palombo M. et al. NeuroImage 2020]. The parameters estimated from the direction-averaged (or spherical mean) data are D_{in}, proxy of the intra-neurite effective axial diffusivity; D_e, proxy of the extracellular effective mean diffusivity; r_s, a proxy of apparent soma radius as well as the signal fractions subject to the constraint $f_{in} + f_{is} + f_{ec} = 1$, proxy respectively of the relaxation-weighted neurite, soma and extracellular volume fractions. The bulk diffusivity inside the sphere D_{is} is fixed to 3 $\mu m^2/ms$. The parameters were fitted using a Random Forest regression algorithm (TreeBagger Matlab®) with 200 trees, trained on simulated data, using the code publicly available at *https://github.com/palombom/SANDI-Matlab-Toolbox-Latest-Release*. The training data consisted of simulated signals for 10^5 parameter combinations, uniformly sampled: f_{in} and $f_{is} \in [0, 1]$, $D_{in} \in [0.5, 3]$ $\mu m^2/ms$, $D_e \in [0.5, 3]$ $\mu m^2/ms$ and $r_s \in [1, 12.5]$ μm. Rician noise with a distribution of standard deviations randomly sampled from the voxels within the brain mask of the noise map obtained using MPPCA denoising was added to account for realistic SNR levels and rectified noise floor. The loss function of the training was the mean squared error between predicted parameters and ground truth values. Model fitting provided maps of f_{in}, f_{is}, f_e, D_{in}, D_e and r_s."

(a) Potential degeneracy between $f_{is}$and r_s. We agree that partial coupling (or degeneracy) between the soma fraction f_{is} and soma radius r_s is possible when the acquisition does not provide strong sensitivity to restricted sphere size (e.g., in the low b-values regime). Our protocol benefits from high b-values (up to 6000 s/mm^2) enabled by the Connectom gradient system, which increases sensitivity to signal attenuation from restricted compartments and reduce the f_{is}-r_s coupling/degeneracy. However, we acknowledge that the specific choice of fixed diffusion timing (in our case δ=7 ms, Δ=24 ms) can further modulate the f_{is}-r_s coupling/degeneracy in a protocol-dependent way. To reflect this appropriately, we now explicitly state that r_s should be interpreted as an "apparent soma radius" under our protocol, and that our inferences focus on relative group differences and spatial patterns rather than absolute histological soma radii.

We have now added a paragraph in the limitations section acknowledging this point.

(b) Dot compartment. We did not include an explicit "dot" (immobile) compartment, because there is no evidence that in human in vivo this is required (see for example very low and negligible contribution provided in Tax C. et al. NeuroImage 2020:

https://www.sciencedirect.com/science/article/pii/S1053811920300215). Accordingly, our fits did not include a dot term, and we now state this explicitly in the Methods. However, we would like to clarify that our fitting method (described in details at *https://github.com/palombom/SANDI-Matlab-Toolbox-Latest-Release*) includes accurately the impact of Rician noise and thus it account for the corresponding rectified noise-floor that very often, in high b-values applications, is mistakenly associated with a "dot" compartment. Therefore, there is no expected bias on the estimated f_{is} and r_s due to not including a "dot" compartment.

(c) Exchange modelling and fixed stick diffusivity. We agree that SANDI, as implemented here, does not explicitly model inter-compartment exchange during the diffusion encoding and uses simplified representations of neurites (sticks), but the intra-stick diffusivity, D_{in}, was not fixed but rather fitted. In diseased or aging tissue, deviations from these assumptions (e.g., altered membrane permeability) may bias compartment estimates. This has been investigated in dept in Schiavi S. et al. HBM 2023 (*https://onlinelibrary.wiley.com/doi/full/10.1002/hbm.26416*), so we refer the redear to that. We have added an explicit limitation statement noting that HD-related microstructural changes (e.g., changes to membrane permeability) could affect model parameter fidelity, and thus $f_{is}$and r_s should be treated as MRI-derived effective indices rather than direct quantitative measures of neuron loss or glial hypertrophy. Importantly, our analysis compares groups under an identical acquisition and fitting pipeline, so grouplevel contrasts remain informative even if absolute parameter values are biased.

(d) Robustness / identifiability checks. We agree that reporting robustness strengthens confidence, particularly given subtle effects and biological heterogeneity. The SANDI Matlab Toolbox we used extensively investigates model parameters robustness and identifiability using numerical simulations and synthetic signals accounting for the specific experimental protocol and noise distribution. An example of the results supporting the robustness / identifiability is reported in the Author response images. These results show that accuracy and precision of all SANDI model parameters, except D_{in}, is very high (>~80%, Author response image 1)

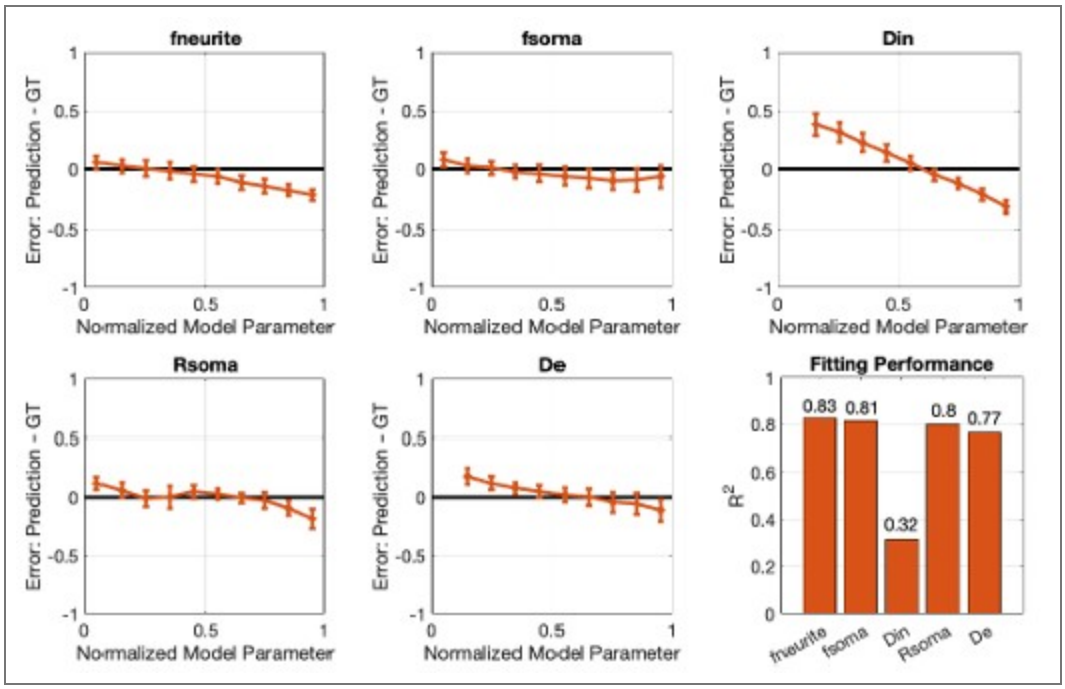

Author response image 1. Analysis of the accuracy and precision of SANDI model parameters estimation. We simulated 10^4 synthetic diffusion signals using the SANDI model with random combinations of five parameters: $f_{neurite}(f_{in})$, $f_{soma}(f_{is})$, D_{in}, $R_{soma}(r_s)$, and D_e. Parameters were sampled uniformly from: $f_{neurite}$, $f_{soma} \in [0,1]$; D_{in}, D_e $\epsilon[0.5,3.0]$ $\mu m^2/ms$; R_{soma} $\epsilon[1,12]$ μm. Rician noise with experimentally estimated variance was added, and the SANDI model was then fit to the noisy signals. For each parameter, we report the relative percentage error between estimated and ground-truth values as a function of the parameter value (normalized to [0,1]), together with goodness-of-fit (R^2).

and sensitivity to changes as small as 5% in each of the model parameters is correctly captured (Author response image 2A), with small to negligible degeneracy (except, once again, for D_{in}), even in presence of exchange (Author response image 2B).

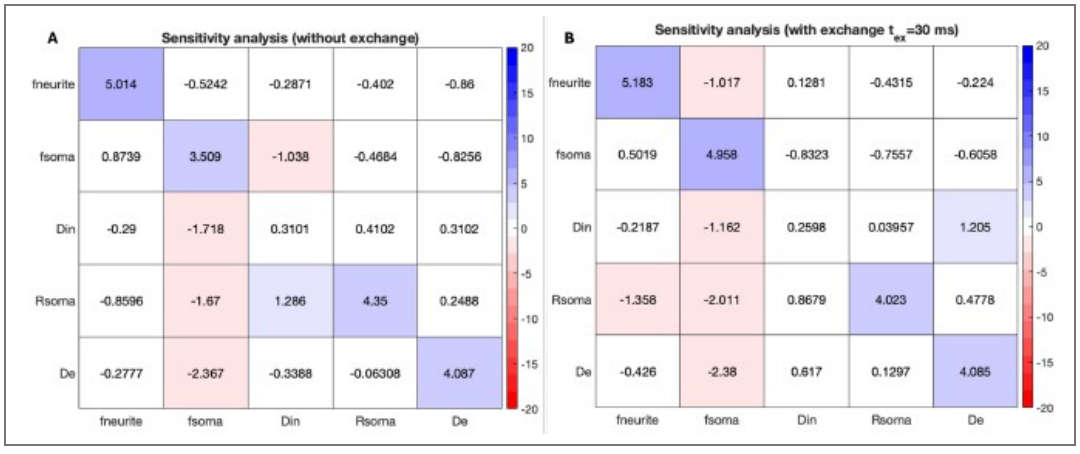

Author response image 2. Sensitivity to 5% parameter modulations. The matrices show how a controlled perturbation in one parameter propagates into the estimated values of all model parameters. Each row corresponds to a 5% increase in the parameter on the y-axis; the resulting percentage change observed in each estimated parameter is reported along the x-axis. An ideal estimator would yield a purely diagonal matrix, with 5% on the diagonal and 0% elsewhere (no cross-talk). In (A), we used the same synthetic SANDI signals as in Figure 1. In (B), we additionally generated 10^4 synthetic signals incorporating neurite–extra-cellular exchange using the

NEXI model [*https://doi.org/10.1016/j.neuroimage.2022.119277*] and an exchange time representative of human cortex (τ_{ex} ≈ 30 ms) [*https://doi.org/10.1162/imag_a_00104*].

We have therefore revised the manuscript language to be more precise and appropriately cautious, describing f_{is} and r_s as apparent compartment indices and explicitly discussing potential confounds (e.g., parameter coupling, and unmodelled exchange), while clarifying the value of SANDI for detecting reproducible group-level microstructural differences in HD.

> *(6) Clarify "not-classified" group in figures:*
>
> *It is not clear to me what the "not-classified" groups shown in Figures 3-4 represent, what criteria determined their inclusion, and whether their inclusion affects the comparability or interpretability of staging-based analyses*

We have added to the legends of Figures 3 and 4 that not-classified refers to HD participants who could not be HD-ISS classified due to missing clinical data or their CAG repeat falling within the 36-40 range. As correlation analyses were conducted across the whole HD sample though, these datapoints were included in the scatterplot.

> *(7) Figure labeling:*
>
> *There appears to be a mismatch between figure numbering and captions around Figures 3-4. Please ensure alignment.*

Mismatch between figure numbering and captions has been corrected.

> *Minor suggestions:*
>
> *(1) Figures 1-2:*
>
> *(a) Label axis values meaningfully, e.g., negative vs. positive instead of 0 vs 1.*
>
> *(b) Add units to MD axes (e.g., ×10⁻⁴ mm²/s).*
>
> *(c) Figure 6 colors: Consider improving the color distinction between "Age" and "fis" predictors, which are currently hard to differentiate.*

The suggested adjustments have been made to Figures 1, 2, 5 and 6 and Figure 2 legend.

> *(c) Discuss why apparent soma size decreases in some ROIs (e.g., pallidum), if unexpected.*

We offer the following speculation about the reduced soma size in the pallidum (pages 20/21): Changes in apparent soma size may reflect alterations in neural and glial cell proportions and/or morphology, including astrocyte and microglia swelling in response to neurodegeneration and soma shrinkage preceding neuronal cell death. Thus, increased apparent soma size in the striatum may indicate HD-related reorganisation of cell types driven by MSN loss and reactive glial cell swelling, whereas smaller soma size in the pallidum may result from infiltration of smaller glia cells prior to secondary neuronal loss following striatal MSN degeneration.

> ***Reviewer #3:***
>
> *(1) An important question is whether the SANDI measures, which require an expensive scanner and elaborate processing, are better biomarkers than the more traditional DTI measures. Can the authors compare the effect size of FA/MD with SANDI measures? In some of the plots and tables, FA/MD seem to have comparable, if not higher, correlations with QMotor or CAP scores. On the same vein, it is unclear whether DTI measures were included in hierarchical stepwise regression. I wonder if the stepwise models may have*

> *picked up FA/MD instead of SANDI measures if they are given a chance. Overall, I hope the authors can discuss their findings also in this light of cost vs. benefit of adopting SANDI in future studies, which is an important topic for clinical trials.*

Effect sizes (ES) of group differences in all microstructural indices can be found in Table 4. ES of DTI and SANDI indices in the caudate and putamen were broadly comparable with a trend for MD showing larger ES (FA: r_{rb} = 0.38 -0.55, MD: r_{rb} = 0.51 -0.61, f_{is}: r_{rb} = 0.32 -0.45, r_s: r_{rb} = 0.45 0.53).

This information is now reported in the result section on pages 15/16 and is being discussed in light of cost versus benefit considerations on pages 21 and 25.

> *(2) Similar to the above point, it is very important to consider how strong the biomarking signal is from SANDI measures compared to the good old striatal volume. Some plots seem to indicate that volumes still have the highest correlation with QMotor and the highest effect size in group comparisons. It would be helpful for the community to know where the new SANDI measures stand compared to the most typically used volumes in terms of effect size.*

Effect sizes (ES) of group differences in volumes can be found in Table 2. ES in caudate and putamen volumes ranged between r_{rb} = 0.49 -0.55 and were comparable to the ES of apparent soma size r_{rb} = 0.45 -0.53 but slightly larger than ES of soma density r_{rb} = 0.32 -0.45.

This information is now reported in the result section on page 15/16 and is being discussed on pages 21 and 25.

> *(3) The diffusion measures are inevitably correlated to some degree. Please provide a correlation matrix in the supplementary material, including all DWI measures, to enable readers to better understand how similar SANDI measures are to each other or vs. other DTI measures. Perhaps adding volumes to this correlation matrix may also be a good future reference.*

We have added cross-correlation matrices between all imaging measures (SANDI, DTI, Volumes) for the total sample as well as for HC and HD participants separately to the Supplementary material (Figure 3), providing an overview of the shared variance within SANDI parameters and between SANDI and DTI and volume metrics for each group.

> *(4) ISS stages:*
>
> *(a) The online ISS calculator requires cut-offs derived from the longitudinal Freesurfer pipeline, while the authors do not have longitudinal data. Thus, the ISS classification might be inaccurate to some degree if the authors used the FS cross-sectional pipeline. Please review this issue and see if updated cut-offs should be used to classify participants.*

We acknowledge that our HD-ISS classifications may have been biased due to the use of crosssectional rather than longitudinal FreeSurfer v6 volumes (page 23).

> *(b) Were there really no participants with ISS 0 among the 56 HD individuals? Please clarify in the manuscript.*

We classified four individuals as ISS 0 based on their caudate and/or putamen z-scored volumes falling below 2SD of the healthy control mean. These analyses are described on pages 14-15 and were based on the cross-sectional data of this study.

> *(5) A note on terminology that might be confusing to some readers. According to the creators of ISS, the ISS stages are created for research only; they are not used or applied in the clinic. On the other hand, the terms "premanifest" and "manifest" have a clinical*

> *meaning, typically based on the diagnostic confidence level. The assignment of ISS0-1 to premanifest and ISS2-3 to manifest may create some non-trivial confusion, if not opposition, in some segments of the HD community. The authors can keep their current terminology, but will need to at least clarify to the reader that this assignment is speculative, does not fully match the clinically-based categories, and should not be confused with similarly named groups in the previous literature.*

To avoid confusion about terminology, we have removed the labels "premanifest" versus "manifest" throughout the manuscript. We refer to HD-ISS 0-1 and HD-ISS 2-3 when referring to the exploratory comparisons between HD-ISS stages.

> *(6) The population in the study seems to be obtained from different other studies or research projects, and there are missing scores for several participants due to the retrospective nature of sample gathering for the analyses. Please state clearly that this study was done with retrospective data to properly justify why there are missing data. Also, and this is important, please clarify for the reader whether there was any temporal bias in the acquisition of data of a certain group (HD) vs. another (HC). It is important to rule out that there were no scanner changes or upgrades that may confound the reported group differences.*

We can confirm there were no Connectom scanner changes or upgrades that may have confounded the reported group differences. This was added to the image acquisition section on page 10. We have added to the participant section on page 9 that data were retrospectively pooled from separate studies and explain this was the reason why HD-ISS classification was only available for a subset of participants.

> *(7) Several of the significant results with SANDI scores seem to be driven by a subgroup of HD individuals that are more clearly different than the healthy control distribution. Not sure if this may help, but one idea the authors can consider is to check if HD individuals that deviate more than 2 SDs from the healthy control distribution of SANDI scores have also worse QMotor, worse atrophy, or higher CAP scores than those HD individuals that are practically within the 2SD boundary distribution of HDs. This is another way of showing that the new measures have potential for application in individualized medicine (the MRI Z score of a patient as a proxy of the clinical deterioration). It is not a request to authors but just a suggestion for their consideration.*

The data points in the scatterplots of Figures 3, 4, and 7 have now been color-coded according to HD-ISS stage, showing a stage-related worsening of microstructural and volumetric imaging markers and Q-Motor performance.

> *(8) The variance explained in hierarchical regression is obtained by fitting models within the sample, and can be subject to overfitting. In the absence of a more robust cross-validated R2, the authors may want to at least briefly inform the reader that the current approach can be subject to overfitting and does not represent a true out-of-sample R2.*

We have added this point to the study limitations in the Discussion section on page 23.

> *(9) There are two Figure 3 labels, and all figures thereafter do not match the manuscript.*

The Figure numbering has been corrected.

> *(10) In (the currently labelled) Figure 8, there seem to be fewer than 56 data points in the scatterplots. Is there a reason why not all 56 HD individuals do not have the CAP100 score available? CAP needs only CAG and age, which all HD gene carriers should have, to be included in the study.*

Inclusion criteria for individuals with HD for the HD-DRUM project were a positive genetic test for the presence of the mutant huntingtin allele (CAG length ≥ 36 repeats) and/or a clinical diagnosis of HD. Thus, for a small number of participants CAG was not available for the calculation of CAP100 score.

https://doi.org/10.7554/eLife.107661.2.sa0